ISSN 0915-633X

NATIONAL INSTITUTE FOR FUSION SCIENCE

Comprehensive Simulation Study on Local and Global Development of Auroral Arcs and Field-Aligned Potentials

T. Watanabe, H. Oya, K. Watanabe and T. Sato

(Received – Sep. 29, 1992)

NIFS-195 Oct. 1992

RESEARCH REPORT
NIFS Series

NAGOYA, JAPAN

Comprehensive Simulation Study on Local and Global Development of Auroral Arcs and Field-Aligned Potentials

TOMOHIKO WATANABE AND HIROSHI OYA

Geophysical Institute, Tohoku University, Sendai 980, Japan

KUNIHIKO WATANABE AND TETSUYA SATO

Theory and Computer Simulation Center, National Institute for Fusion Science, Nagoya 464-01, Japan

Abstract

Extensive three-dimensional computer simulations of the magnetosphere-ionosphere (M-I) coupling are performed to study self-excitation of auroral arcs with special emphasis on 1) nonlinear evolution of the feedback instability in the M-I coupling system, 2) controlling mechanisms of the auroral arc structure, 3) formation of a field-aligned electric potential structure in association with the development of the feedback instability, and 4) effects of the parallel potential generation on auroral arc development. As was already shown by *Sato* [1978] and *Watanabe and Sato* [1988], it is reconfirmed that the feedback instability produces a longitudinally elongated, latitudinally striated structure where the upward field-aligned current and the ionospheric density are locally enhanced. On top of this the present extended study reveals the following important new features : 1) The global distribution of the striation structure is primarily governed by the magnetospheric convection pattern and the ionospheric density distribution. 2) There appears a significant dawn-dusk asymmetry in the auroral arc formation, even though the apparent geometrical relationship is symmetric. This dawn-dusk asymmetry reflects the geometrical fact that the ionospheric Pedersen current closing the magnetospheric current is anti-symmetric with respect to the noon-midnight plane, while the self-closed Hall current is symmetric. 3) The recombination effect plays a significant role in the global, as well as local, development of the auroral arc structure. The nonlinearity of recombination, in conjunction with the closure of an arc-associated local field-aligned current system, acts to destroy an old arc and creates a new arc in a different but adjacent position. This results in a peculiar behavior of auroral arc formation and deformation. 4) A V-shaped field aligned potential structure is created in association with an auroral arc. Rapid increase in the electron density and the local upward field-aligned current of an arc arises as a result of enhanced ionization by precipitating electrons accelerated by the parallel potential. 5) A drastic oscillatory behavior of appearance and disappearance of auroral arcs is obtained when the ionization effect is strong. The period is primarily given by the Alfvén bounce time.

Keywords: magnetosphere-ionosphere coupling, auroral arc, field-aligned potential, feedback instability, computer simulation, magnetohydrodynamics

1 Introduction

Auroral phenomena in the Earth's polar region are considered to occur in the final stage of the energy transport processes from the solar wind into the ionosphere through the energy conversion processes in the magnetospheric boundary region, the magnetotail, and the acceleration region of auroral electrons. Auroras are in gross classified, according to their activities, in three groups, namely, quiet (pre-breakup), breakup, and diffuse (post-breakup) auroras. The breakup aurora may be associated with the energy conversion processes such as a large and rapid magnetic reconnection process in the magnetospheric tail region and a stimulated field-aligned precipitation process of accelerated electrons. The diffuse aurora may be excited by pitch angle scattered electrons and/or protons in the disturbed magnetosphere. In these auroral activities, the energy conversion processes in the magnetosphere would play a direct role, while the ionosphere is regarded as a passive medium.

The characteristics of quiet auroral arcs such as the multiple striation pattern and the regular quiet motion, however, appear to reflect an intrinsic global feature of the quiet magnetosphere-ionosphere (M-I) coupling system. It is expected therefore that the ionosphere will play an active role in the formation of quiet auroral arcs. Formation mechanisms of quiet auroral arcs were, more than twenty years ago, discussed by means of theoretical models for the M-I coupling system [*Atkinson*, 1970; *Ogawa and Sato*, 1971; *Sato and Holzer*, 1973]. Since then, *Sato* [1978] developed a self-contained theory of quiet auroral arcs that quiet auroral arcs develop as a result of a spontaneous feedback instability between the lossless reactive magnetosphere with a convection flow and the dissipative ionosphere with no energy source. More specifically, the coupled magnetosphere and ionosphere system becomes feedback unstable under a certain condition when the magnetospheric waves, i.e., Alfvén and magnetosonic waves, are coupled with the ionospheric waves, electrostatic waves.

Based on the feedback theory, formation of auroral arcs was studied by means of two dimensional computer simulations [*Miura and Sato*, 1980], where the role of the magnetosphere was modeled as a lumped circuit. Multiple auroral arcs were observed to develop on the night side of the auroral zone. The first full comprehensive three-dimensional dynamic simulation of auroral arc formation was then performed by *Watanabe and Sato* [1988]. They solved the magnetohydrodynamic (MHD) equations for the magnetosphere and the two-fluid equations

for the ionosphere, self-consistently, in a three dimensional M-I coupling system, and showed that a longitudinally elongated striation structure of the field-aligned current and ionospheric density develops as a result of the feedback instability. Many features of the striated structure are in good agreement with those of quiet auroral arcs [*Park and Cloutier*, 1971; *Cloutier et al.*, 1973; *Casserly and Cloutier*, 1975; *Sesiano and Cloutier*, 1976].

In the present study, we first carry out a long time simulation run to examine the nonlinear evolution of the feedback instability using the code developed by *Watanabe et al.* [1986] and *Watanabe and Sato* [1988]. Second, changing the flow pattern of the plasma convection in the magnetospheric equator, we investigate how the global distribution of the current and density striation structures depend on the magnetospheric convection pattern and the ionospheric density distribution.

Thirdly, we devote ourselves to studying the formation of a parallel potential along the auroral field lines and to investigating the ionization effect in the ionosphere on the auroral arc formation. With the development of the feedback instability, we assume that the ion acoustic wave instability arises as a result of the local enhancement of the striated field-aligned current system, thereby generating an anomalous resistivity and, hence, a parallel electric field [*Sato and Okuda*, 1980]. Nonlinear generation of the parallel anomalous resistivity in an electrically coupled M-I system implies the change of the dynamical response of the whole feedback system. It is known that the feedback instability is most unstable when the electric potential wave in the ionosphere leads by $\pi/2$ in phase to the field-aligned current wave associated with the magnetospheric Alfvén wave in the M-I coupling system; i.e., when the magnetospheric response is purely inductive [*Sato*, 1978]. Thus, the nonlinear growth of quiet auroral arcs due to the feedback instability is expected to be stabilized by the nonlinear phase shift due to the appearance of parallel resistivity. Contrary to the stabilizing effect due to the parallel resistivity, the development of auroral arcs can be activated by the formation of field-aligned potentials, because the potential difference accelerates the precipitating magnetospheric electrons and results in local enhancement of ionization and excitation of the ionospheric neutral atoms and molecules. We thus investigate how quiet auroral arcs are formed in a nonlinear M-I coupling system where both the parallel anomalous resistivity and the ionization effect are taken into account.

The numerical models and procedures are given in the next section. The nonlinear evolution

and global distribution of the density and current striation structures are shown in section 3 where the parallel resistivity and the ionization effect are discarded. In section 4, shown are the simulation results where the field-aligned resistivity and the ionization effect are both taken into account. Summary is given in section 5.

2 Numerical Model and Procedure

2.1 Governing Equations and Boundary Conditions

The numerical model of the M-I coupling system in the present study is essentially the same as those of the previous works [*Watanabe et al.*, 1986; *Watanabe and Sato*, 1988]. Thus, only important portions are briefly reviewed here. A radially extended magnetic field model is employed to represent the magnetic field in a M-I coupling system (see Fig.2 in *Watanabe et al.*[1986]). A spherical coordinate system (r, θ, φ) is defined in the simulation box where the center of the Earth is located at $r = 0$; the $\theta = 0$ and $\varphi = 0$ axes point to the north pole and the midnight, respectively. The governing equations describing the dynamics of the magnetosphere are given by the MHD equations;

$$\frac{\partial \vec{B}}{\partial t} = -\nabla \times \vec{E} \tag{1}$$

$$\frac{\partial \vec{v}}{\partial t} + (\vec{v} \cdot \nabla)\vec{v} = \frac{1}{\rho_0}(\vec{j} \times \vec{B}) \tag{2}$$

$$\vec{E} = -\vec{v} \times \vec{B} + \eta j_{\parallel} \hat{r} \tag{3}$$

$$\mu_0 \vec{j} = \nabla \times \vec{B} \quad . \tag{4}$$

Here, $\vec{B}$, $\vec{v}$, $\vec{E}$, and $\vec{j}$ are the magnetic field, the velocity of the plasma flow, the electric field, and the current density, respectively; ρ_0 is the mass density, which is given by a function of r only; μ_0 is the permeability; η and $j_{\parallel}$ are the parallel anomalous resistivity and the field-aligned current density; $\hat{r}$ denotes the unit vector in the radial direction. The parallel resistivity η is modeled based on the quasi-linear theory of the ion acoustic wave, as will be shown in section 2.2.

The ionospheric equations are defined on the spherical surface at $r = R_E$ where R_E is the Earth's radius as the height-integrated ionospheric equations obtained from the two-fluid

equations [*Sato*, 1978]. They are

$$\frac{\partial N}{\partial t} + \frac{\vec{E}_I \times \vec{B}_I}{B_I^2} \cdot \nabla_\perp N = \frac{j_I - j_{I0}}{eh} - \alpha(N^2 - N_0^2) + \frac{\gamma}{eh} j_{hot} \quad , \tag{5}$$

and

$$\vec{I}_I = ehM_P N \vec{E}_I - ehM_H N \frac{\vec{E}_I \times \vec{B}_I}{|\vec{B}_I|} \quad , \tag{6}$$

where $\vec{E}_I$, $\vec{I}_I$, N are the ionospheric electric field, the height-integrated current in the ionosphere, and the height-averaged number density, respectively; j_I is the field-aligned current density at the ionospheric height; $\vec{B}_I$ is the ionospheric magnetic field, which is assumed to be constant; j_{I0} and N_0 are the values of j_I and N in the equilibrium state, respectively; α is the recombination rate; e, M_P, and M_H are the elementary charge and the Pedersen and Hall mobilities, respectively; h denotes the effective height of the ionosphere; γ and j_{hot} are the electron-ion pair production rate and the field-aligned current density carried by precipitating hot electrons, which are given in section 2.2.

The magnetospheric and ionospheric equations are self-consistently closed by the current continuity relation between the field-aligned magnetospheric current and the field-crossing (line-tying) ionospheric current; i.e.,

$$\nabla_\perp \cdot \vec{I}_I = -j_I \quad . \tag{7}$$

The ionospheric equations are numerically solved at every time step, and give the boundary condition for the electric field at $r = R_E$. The boundary condition on the magnetospheric equatorial plane located at $r = 10R_E$ is such that the magnetic field and the plasma flow are unchangeable with time. A stationary large-scale convection in the magnetospheric equator provides a constant large-scale perpendicular electric field distribution, which drives a large-scale field-aligned current; the convection pattern is changed from case to case to study the characteristics of the distribution pattern of auroral arcs. The latitudinal boundaries of the simulation box are defined by the geomagnetic surfaces at 70° and 72° in latitude, i.e., $\theta = 20\pi/180$ and $\theta = 18\pi/180$. At the latitudinal boundaries, any plasma flows across the boundaries are prohibited, i.e., $v_\theta = 0$ at $\theta = 18\pi/180$ and $20\pi/180$. The boundary conditions for other variables are summarized as follows; $\partial B_r/\partial\theta = 0$, $B_\theta = 0$, $\partial(B_\varphi \sin\theta)/\partial\varphi = 0$, $\partial v_r/\partial\theta = 0$, and $\partial(v_\varphi \sin\theta)/\partial\varphi = 0$ (see *Watanabe et al.*,[1986]).

The magnetic field strength B is given by $B = B_I(R_E/r)^2$, so that the curvature effect is neglected. The radial profile of the mass density ρ_0 is defined in such a way that the

Alfvén velocity is constant everywhere. This implies that no partial reflection along the field lines is allowed. The ambient height-averaged density in the ionosphere is given by $N_0 = N_{night} + (N_{noon} - N_{night})(1 - \cos\varphi)/2$, where N_{night} and N_{noon} are the ionospheric density at $\varphi = 0$ and π, respectively. Physical parameters used in this work are summarized in Table 1. Numerical models for the parallel anomalous resistivity η, the electron-ion pair production rate γ and the part of the field-aligned current density carried by hot electrons j_{hot} are explained in detail in the next subsection 2.2.

2.2 Models of parallel resistivity and ionization effect

As the origin of the parallel resistivity, we assume a quasi-linear diffusion of ion acoustic waves which are excited by a current driven instability. When the field-aligned current density $j_{\parallel}$ becomes larger than a certain critical current density for the ion acoustic instability, the parallel resistivity η is given by (see Appendix)

$$\eta = \eta_0 (\frac{j_{\parallel} - j_c}{\Delta j})^2 \qquad for \;\; j_{\parallel} > j_c \quad , \tag{8}$$

where η_0 is a parameter to determine the magnitude of η; Δj is a normalizing current which is set to be $1\mu A/\mathrm{m}^2$, here; the critical current density j_c is a given function of r, which is determined in the following manner. The necessary condition for the current-driven ion acoustic instability is given by

$$V_d > C_s\{1 + (\frac{m_i}{m_e})^{1/2} (\frac{T_e}{T_i})^{3/2} \exp[-\frac{T_e}{2T_i}]\} \tag{9}$$

[*Ichimaru*, 1973]. Here, V_d is the average velocity of the current carrying electrons; m_i and m_e are the ion and electron mass; T_i and T_e are the temperatures of ions and electrons, respectively; C_s is the ion acoustic velocity, $(T_e/m_i)^{1/2}$. The critical velocity for the instability depends exponentially on T_e/T_i due to the ion Landau damping effect. Thus, the ion acoustic wave can be excited when $T_e/T_i \gg 1$ and $V_d > C_s$. The value of T_e/T_i changes along auroral field lines; $T_e/T_i \sim 1$ in the ionosphere, while $T_e/T_i < 1$ in the plasma sheet. In a certain height region between the ionosphere and the magnetospheric equator, it is likely that the condition of $T_e/T_i \gg 1$ is realized by some kinetic effects, e.g., an anomalous electron heating due to wave-particle interactions and the difference of the mirror points between hot plasma sheet electrons and ions. We presume that the region $T_e/T_i \gg 1$ corresponds to the acceleration

region of auroral particles. Accordingly, we choose the following model for the critical current density j_c as a function of r [*Lysak and Dum*, 1983];

$$j_c(r) = j_{c0}(\frac{R_E}{r})^2\{1 - c_1 \exp[-\frac{(r/R_E - c_3)^2}{c_2}]\} \quad , \tag{10}$$

where $c_1 = 0.5$, $c_2 = 16$, and $c_3 = 3$; j_{c0} is set to be $22.5\mu A/\mathrm{m}^2$. We assume that the ion acoustic instability can not be caused by cold and up-going ionospheric electrons which carry the downward field-aligned current. Thus, the parallel anomalous resistivity arises only in the region where the upward field-aligned current density becomes larger than the critical current density j_c.

A field-aligned potential difference, Ψ, which is defined as $\Psi = |-\int \eta j_{\parallel} dr|$, is formed in consequence of generation of parallel resistivity. Low energy electrons are accelerated by Ψ to the energy level of $e\Psi$ in parallel to the magnetic field. When the accelerated electrons precipitate down into the ionosphere, the plasma density in the ionosphere is increased by the ionization of neutral atoms and molecules. The maximum number of atoms and molecules ionized by one precipitating electron is given by Ψ/Ψ_{ion}, where Ψ_{ion} denotes the averaged ionization potential. Neutral atoms and molecules cease to be ionized when $\Psi < \Psi_{ion}$. Consequently, we adopt a model for the electron-ion pair production rate γ as a function of Ψ as follows;

$$\gamma = \frac{\Psi}{2\Psi_{ion}}[\tanh(\frac{\Psi - \Psi_{ion}}{\Delta\Psi}) + 1] \quad . \tag{11}$$

Here, Ψ_{ion} and $\Delta\Psi$ are set to be $15V$ and $2.5V$, respectively. Regarding the part of the field-aligned current density carried by accelerated electrons j_{hot}, we consider that the kinetic energy flux of accelerated electrons $e\Psi \cdot j_{hot}/e$ is proportional to the macroscopic Joule heating $\Psi j_{\parallel}$ in the acceleration region. Then, the current density of hot electrons is given by

$$j_{hot} = \varepsilon j_{\parallel} \quad . \tag{12}$$

Here, ε is defined in the range of $0 \leq \varepsilon \leq 1$. From the above discussion, we obtain an explicit representation of the ionization term in Eq.(5) as follows;

$$\frac{\gamma}{eh} j_{hot} = \varepsilon \frac{j_I}{eh} \frac{\Psi}{2\Psi_{ion}}[\tanh(\frac{\Psi - \Psi_{ion}}{\Delta\Psi}) + 1] \quad . \tag{13}$$

By changing the values of η_0 and ε, we investigate the formation of auroral arcs with the field-aligned potential and the ionization effect.

2.3 Numerical Procedure

The simulation box consists of the $82 \times 56 \times 38$ grid-point system in the (r, θ, φ) coordinates. The governing equations are transformed into the finite difference equations. Since the magnetic field is so strong in the ionosphere, we assume that the ionospheric electric field can be expressed by $-\nabla\Phi$ using an electrostatic potential Φ. On substituting Eq.(6) into Eq.(7), we obtain an elliptic equation for Φ. At every time step, the two-dimensional elliptic equation is solved along with the three-dimensional MHD equations. Time integration of Eqs.(1)-(4) and (5) are carried out by the fourth order Runge-Kutta-Gill (RKG) method [*Watanabe and Sato*, 1990]. The simulation procedure is divided into two stages as has been adopted in the previous work [*Watanabe and Sato*, 1988]. First, we obtain an almost equilibrium (ambient) solution which is consistent with a given convection pattern of the plasma flow in the magnetospheric equatorial plane. In this initial stage Eqs.(1)-(4) and (6)-(7) are solved for the given distributions of the magnetospheric and ionospheric plasma densities and the Earth's magnetic field. After several bounce motions of Alfvén waves between the magnetosphere and the ionosphere, the initial equilibrium state for the main stage is obtained in the simulation system. Next, in the main stage, we solve the whole set of Eqs.(1)-(7) including the equation governing the time evolution of the ionospheric density.

3 Simulations without ionization : Dark arcs

3.1 A long time simulation run : Standard case

We have carried out a long time simulation run to study the nonlinear evolution of the feedback instability under the almost same condition as the previous work [*Watanabe and Sato*, 1988]. The Pedersen and Hall mobilities used in the present simulations are larger than those of the previous work. Thus, we need more time steps to obtain an initial equilibrium state, which is attained at about $t = 15\tau_A$, because the Alfvén waves are reflected at the ionosphere more strongly than for the previous work. A twin-vortex convection with the vortex centers at MLT = 6 and 18 (where MLT denotes the magnetic local time) is set in the magnetospheric equator. The distribution of the electric potential in the ionosphere obtained from the initial stage of the simulation is naturally the same as that of the equatorial electric potential pattern

(see Figure 4 (a)). From this initial stage we go into the main stage of the simulation, in which Eq.(5) is solved to determine the development of the ionospheric density.

Developments of the ionospheric number density and the field-aligned current density are shown in the left and right panels of Figures 1(a)-(c), respectively. Their deviations from the equilibrium state are represented by contours of solid (increment) and dashed (decrement) lines at (a) $t = 11.28\tau_A$, (b) $t = 16.93\tau_A$, and (c) $t = 22.57\tau_A$. We note that the distributions at $t = 11.28\tau_A$ correspond to those of the last period of the previous simulation [*Watanabe and Sato*, 1988]. The distributions of longitudinally elongated density and current striations are as a matter of course very similar to the previous results. We call the striated structure with $\tilde{n} > 0$ and $\tilde{j}_{\parallel} > 0$ as a 'positive dark arc' and that with $\tilde{n} < 0$ and $\tilde{j}_{\parallel} < 0$ as a 'negative dark arc', since the field-aligned current is carried by normal electrons, hence, neither the electron-ion pair production nor excitation take place. Here, $\tilde{j}_{\parallel}$ and $\tilde{n}$ denote the time dependent components of j_I and N; $j_I = j_{I0} + \tilde{j}_{\parallel}$ and $N = N_0 + \tilde{n}$. After $t = 11.28\tau_A$, an apparent positive dark arc near at MLT = 3 rapidly grows until the increments of the ionospheric number density and the upward field-aligned current density are maximized at about $t = 16\tau_A$. At this time, the increment of the number density and the decrement of the ionospheric electric field intensity in the positive dark arc reach to 90 % and 60 % of their ambient values at the equilibrium state, respectively. The perturbation of the upward field-aligned current, simultaneously, increases to $3\mu A/\mathrm{m}^2$. A contour plot of the ionospheric density perturbation in latitude-time diagram at MLT = 2.84 is shown in Figure 2. The striated structure with the latitudinal width of about 30km makes a drift in the direction of the Pedersen current (poleward) at the speed of about 10 m/sec. When the growth of the density and current striations at MLT = 2.84 is saturated at about $t = 16\tau_A$, the main positive dark arc in the post-midnight sector appears to shift eastwards at an apparent speed of 1 to 2 km/sec as is seen by comparing Figures 1(b) and (c). Following this rapid shift, a new pair of positive and negative dark arcs are born on the lower latitude side (at about 71.7° in latitude).

We shall pay attention to this nonlinear development of dark arcs in the post-midnight sector and attempt to reveal the governing nonlinear mechanism. The ionospheric density near at MLT = 3 locally decreases in association with an apparent eastward shift of the positive dark arc. In order to confirm the direct cause of the local damping of the positive dark arc, we show the time development of the main source and sink terms in Eq.(5) at MLT = 3 and

71.64° in latitude in Figure 3, in which $\tilde{j}_{\parallel}/eh$, $-2\alpha\tilde{n}N_0$, $-\alpha\tilde{n}^2$ and $-\alpha\tilde{n}(\tilde{n}+2N_0)$ are plotted. The convection term of Eq.(5) due to $\vec{E}_I \times \vec{B}_I$ drift is much smaller than those terms. It can be seen in Figure 3 that when the feedback instability fully develops at $t = 16\tau_A$, the nonlinear recombination term, $-\alpha\tilde{n}^2$, becomes important and occupies about 30 % of the total recombination rate, $-\alpha\tilde{n}(\tilde{n}+2N_0)$. Thus, it is inferred that the positive dark arc is prohibited from growing by enhancement of the nonlinear recombination rate and decays near at MLT = 3. The apparent rapid eastward shift is not the real motion of the dark arc, but rather reflects the suppression of the original pair of positive and negative dark arcs and the generation of a new pair on the east side, that is, the shift of the unstable region due to the nonlinear change of the environmental condition such as the ionospheric density, field-aligned current and electric field distributions. Because of this environmental change, another pair of positive and negative dark arcs are born on the eastward of the original disappearing positive dark arc.

The nonlinear recombination term, $-\alpha\tilde{n}^2$, is expected to play some role in generating the secondary positive dark arc on the equator side of the primary one. In the density depleted region (negative dark arc) where $\tilde{n} < 0$ and $\tilde{j}_{\parallel} < 0$, the nonlinear recombination term acts to reduce the linear recombination term, $-2\alpha\tilde{n}N_0$. As is shown in Figures 1 and 2, the negative dark arc between the primary and secondary positive dark arcs survives, while the primary positive dark arc decays out near at MLT = 3. On the other hand, the latitudinal (θ) and longitudinal (φ) components of the left hand side of Eq.(7) satisfy the inequality;

$$|\frac{1}{r\sin\theta}\frac{\partial}{\partial\theta}\sin\theta I_{I\theta}| \gg |\frac{1}{r\sin\theta}\frac{\partial}{\partial\varphi}I_{I\varphi}| \quad , \tag{14}$$

where $I_{I\theta}$ and $I_{I\varphi}$ are the θ and φ components of $\vec{I}_I$, respectively. This means that a local field-aligned current system ($\tilde{j}_{\parallel}$) is almost closed in a meridian plane with a pair of upward and downward field-aligned currents. Thus, after the local damping of the primary positive dark arc (where $\tilde{j}_{\parallel} > 0$), the secondary positive dark arc (where $\tilde{j}_{\parallel} > 0$) can be generated so as to close the surviving downward field-aligned current on the negative dark arc (where $\tilde{j}_{\parallel} < 0$) in the meridian plane at MLT = 3. This implies that the difference of the nonlinear recombination term between the positive and negative dark arcs plays an important role in the nonlinear development of the dark arcs in the feedback coupling system.

3.2 Global distribution of auroral arcs

We shall next investigate the dependence of the global distribution of the ionospheric striated structure on the convection pattern of the magnetospheric equatorial plasma flow. Numerical simulations have been performed for four cases, cases I $\sim$ IV, with different convection patterns in the magnetospheric equator. Equilibrium distributions of the electric potential Φ and the field-aligned current density j_{I0} in the ionosphere are shown in Figures 4 (a)-(d) and color maps of the ionospheric density enhancement (positive dark arcs) at about $t = 11\tau_A$ are shown in Figures 5 (a)-(d), which correspond to cases I to IV, respectively. In order to make visible the fine structure of the striations, the latitudinal width (2 degrees) of the simulation zone is artificially magnified from 2 degrees to 5 degrees in Figures 4 and 5. The simulation zone at $r = 1R_E$ is viewed from a high point in the midnight meridian plane. In Figures 4(a)-(d) the color changes from blue to red as the electric potential changes from negative to positive. Contours of the intensity of the upward and downward field-aligned currents are superposed by white and black lines, respectively, on the color potential plots. Case I shows the basic twin-vortex flow pattern which was given as a standard case in section 3.1. In contrast to the case I where the latitudinal peak of Φ is located at 71.3° in latitude, the peak of Φ of the case II is pushed towards the lower latitude (at 70.7° in latitude). In the cases III and IV, more realistic equatorial convection patterns are given. In the case III, the centers of the vortices are shifted towards the magnetospheric tail region so that the longitudinal peaks of Φ approach to the midnight. In the case IV, a dawn-dusk asymmetric convection pattern is introduced based on satellite and ground-based observations [*Ahn et al.*, 1989;*Kamide et al.*, 1989]. The region of the positive electric potential is longitudinally elongated across the midnight, while the negative potential region with the longitudinal peak at MLT = 16.9 is confined to MLT = 12 $\sim$ 21.8. The latitudinal peak of the electric potential is located at the middle of the simulation zone, i.e., 71° in latitude in the case IV.

Case I

As is shown in Figure 5 (a), longitudinally elongated dark auroral arcs grow preferentially on the high latitude side of the latitudinal peak of the electric potential. Let us divide the whole auroral zone of the ionosphere into four sectors, i.e., the post-midnight sector (MLT = 0 $\sim$ 6), the morning sector (MLT = 6 $\sim$ 12), the afternoon sector (MLT = 12 $\sim$ 18), and

the pre-midnight sector (MLT = 18 $\sim$ 24). A thin longitudinally elongated arc structure most actively develops in the post-midnight sector. The secondary active region is the afternoon sector; the third is the pre-midnight sector where a multiple structure appears; the excitation of the striated structures is most inactive in the morning sector.

Case II

Contrary to the initial condition of the case I, the equilibrium electric field is stronger on the low latitude side than on the high latitude side. The other conditions are the same as those of the case I. As is shown in Figure 5 (b), a multiple density striation structure is formed near at MLT = 19 on the low latitude, while no significant growth of the feedback instability is found in the post-midnight sector. Thus, the global distribution of the dark arcs in the case II differs very much from that in the case I.

Case III

In the case III, the latitudinal peak of the electric potential is located at the same latitude as in the case I. The feedback instability occurs predominantly on the night side, particularly, from the evening to the midnight region as is shown in Figure 5 (c). The distribution of the striated structure reminds us that the active auroral arcs are to be formed in the pre-midnight region, when the upward field-aligned current is carried by hot electrons.

Case IV

One can see in Figure 5(d) that the striated structure is formed mainly in the upward field-aligned current (negative electric potential) region. The active growth of the dark arcs occurs on a slightly high latitude side at about MLT = 14 and on a slightly low latitude side at MLT = 19 $\sim$ 20. No remarkable density enhancement is found in the region of the downward field-aligned current.

As can be seen in the above four simulations, the convection pattern in the magnetospheric equatorial plane governs the global development of the dark auroral arcs. The latitudinal difference of the arc position in the cases I and II clearly reflects the latitudinal shift of the convection pattern. There also appears a dawn-dusk asymmetry in the global arc structure such as the local time dependence of the arc position in the cases I and II. Even if the equatorial

convection pattern is symmetric with respect to the noon-midnight plane, an asymmetry in the arc distribution originates from the asymmetric flow pattern of the ionospheric current which is given by the anti-symmetric Pedersen current and the symmetric Hall current. In other wards, the dawn-dusk asymmetry in the global arc structure is supposed to be caused by different ionospheric responses to the Pedersen and Hall currents. The above simulation results show that the dark arcs grow preferably where the north-south (east-west) components of the Pedersen and Hall current are in the same (opposite) direction. Such is the case for the high latitude side in the post-midnight and afternoon sectors in the case I, the low latitude side in the pre-midnight sector in the case II, and also the high latitude side at MLT $= 12 \sim 16.9$ and the low latitude side at MLT $= 16.9 \sim 21.8$ in the case IV. The ambient density distribution also contributes to determining the global feature of the dark-arc structure on the day side and the night side. Since the larger number density on the day side gives the stronger recombination effect there, the growth of the dark arcs in the afternoon sector is smaller than that in the post-midnight sector for the case I. In addition to the equatorial convection pattern and the ionospheric density and current distributions, the other global conditions, such as the latitudinal inhomogeneity of the convection electric field and the fixed latitudinal boundary condition for the ionospheric perturbation, also would affect the global structure of the dark auroral arcs, since the latitudinal width and the motion of the dark arcs may largely be influenced by these conditions.

4 Simulations with parallel potential generation and ionization : Bright auroral arcs

4.1 Generation of V-shaped parallel potential in the feedback system

Simulations with a parallel resistivity but without ionization are carried out. First, the resistivity parameter η_0 in Eq.(8) is set to be 2.0Ω·km. The other parameters and the convection pattern in the magnetospheric equator are the same as those of the standard simulation shown in section 3.1. Anomalous resistivity arises after $t = 10\tau_A$ at MLT $= 18$ and $71.5°$ in latitude when the condition of $j_{\parallel} > j_c$ is attained. As the field-aligned current grows more and more

through the feedback coupling, the parallel resistivity and the resultant field-aligned potential difference are also generated. Equi-contours of the field-aligned potential difference Ψ defined between the ionosphere and the magnetospheric equator, and the field-aligned current density in the ionosphere j_I are shown in Figures 6(a) and (b) at $t = 29.79\tau_A$. The distribution of Ψ corresponds to the peak of j_I. The latitudinal width of the region where $\Psi > 100V$ is about 10 km at the ionospheric height. The distribution of the perturbed ionospheric density and field-aligned current density at MLT = 18 against the latitude are given in Figures 7(a) and (b). Contour plots of the field-aligned potential and resistivity in the same meridian plane from $r = 1R_E$ through $r = 5R_E$ are also indicated in Figures 7(c) and (d). The field-aligned potential is calculated with the boundary condition that the potential is equal to zero in the ionosphere. The maximum values of the potential difference and the parallel resistivity at $t = 29.79\tau_A$ are $200V$ and 18.8 Ω·m. A V-shaped potential structure is formed along the auroral field lines connecting to an enhanced density and upward field-aligned current in the ionosphere. Thus, the spontaneously excited bright auroral arc in the feedback coupling system is directly associated with the field-aligned potential structure in the arc-associated small-scale current system.

Time evolutions of the ionospheric density, the field-aligned current, and the potential difference at MLT = 18 and 71.5° are shown in Figures 8(a)-(c), respectively, for the cases of η_0 = 0 (solid line), 0.4 (dot-dashed line), 2.0 (dashed line), and 10.0 (dotted line) Ω·km. The case of $\eta_0 = 0$ is the same as the standard simulation shown in section 3.1, thus, no field-aligned potential is formed in this case. The upward field-aligned current for $\eta_0 = 0$ is once saturated at about $t = 17\tau_A$, and again starts to increase. The rapid growth of $\tilde{n}$ and $\tilde{j}_{\parallel}$ after $t = 20\tau_A$ may be caused by nonlinear coupling of the feedback instability in association with merging of two positive dark arcs. A similar growing pattern is observed when the parallel resistivity is introduced. The growth of the upward field-aligned current for $\eta_0 = 10.0$ is suppressed after $t = 15\tau_A$ due to the stabilization of the feedback instability. The saturation level of the upward field-aligned current for $\eta_0 = 10.0$ is about a half of that for the case of $\eta_0 = 0$. As can be seen in Figures 8(a) and (b), the growth of the density and field-aligned current perturbation due to the feedback coupling depends largely on the value of η_0. As η_0 becomes larger, growth of the field-aligned current is more strongly suppressed by the enhanced anomalous resistivity. The potential difference Ψ for $\eta_0 = 0.4\Omega$·km develops to the level of about 70 % of that of

$\eta_0 = 10\Omega$·km at $t = 30\tau_A$. Thus, the actual potential difference dose not so largely depend on the magnitude of η_0.

4.2 Stabilization by nonlinear phase-mismatching

In order to discuss the nonlinear saturation of the feedback instability, we estimate the characteristic impedance of a longitudinally elongated current system of an auroral arc in the M-I coupling system, based on a lumped circuit model. The magnetospheric impedance consists of the inductance $L = \mu_0 l$, the capacitance $C = l/\mu_0 V_A^2$ [*Sato and Holzer*, 1973], and the field-aligned anomalous resistance $R_A = \eta_A l'/\xi^2$. Here, l denotes the field line length between the ionosphere and the magnetospheric equator; V_A is the Alfvén velocity; η_A and l' are the typical magnitude and the field-aligned scale length of the resistivity; ξ is the latitudinal width of the upward field-aligned current perturbation in the ionosphere. In our simulation model, L and C are equal to 72.04 H and 45.62 F. In the case of $\eta_0 = 2\Omega$·km, the anomalous resistivity at $t = 15\tau_A$ has developed into about 3 Ω·m with the field-aligned scale length (half width) of about 5,000 km (see Figure 7(d)) and the latitudinal width of 10 km at the ionospheric height. Then, we can estimate that the field-aligned resistance is $R_A = 0.15\Omega$.

The usual transmission line analysis is applicable to the feedback coupling when R_A is constant. Estimation of the characteristic impedance of the magnetosphere is meaningful to understand the saturation mechanism of the feedback instability, although R_A depends nonlinearly on $j_\parallel$ in our simulation model. The characteristic impedance ζ is given by

$$\zeta = \mu_0 V_A [1 + (\frac{R_A}{\omega L})^2]^{1/4} e^{i\frac{\varphi_0}{2}} \quad , \tag{15}$$

where $\varphi_0 = -\tan^{-1}(R_A/\omega L)$; ω ($\sim \pi/\tau_A$) denotes the angular frequency of the Alfvén wave in the M-I coupling system. The above equation can be reduced to $\zeta = \mu_0 V_A$ when $R_A = 0$. From the values of R_A, L, and ω, R_A is much smaller than ωL. Then, the imaginary part of ζ is approximated by $Im(\zeta) \sim -\mu_0 V_A (R_A/2\omega L)$ for $R_A \ll \omega L$, while the magnitude of ζ is estimated to be $|\zeta| \sim \mu_0 V_A [1 + (R_A/2\omega L)^2]$. The increase of $|\zeta|$ due to the generation of the field-aligned resistivity is smaller than $|Im(\zeta)|$. Thus, $Im(\zeta)$ is more important to stabilize the feedback instability than $|\zeta|$ when $R_A \ll \omega L$. Generation of $Im(\zeta)$ leads to the situation that the phase lag of the field-aligned current with respect to the electric potential becomes smaller than the phase lag of $\pi/2$ that gives the most unstable condition. Then, the growth rate of the

feedback instability is reduced by $Im(\zeta)$ and the instability is weakened. Therefore, the larger the coefficient η_0 is, the lower the saturation level of the instability becomes.

4.3 Ionization effect

The field-aligned potential difference can accelerate auroral electrons along the field line. When the accelerated electrons precipitate down into the ionosphere, they ionize neutral atoms and molecules and increase the plasma density. Therefore, it is required to include the ionization effect in our simulation model. Two typical simulation runs are carried out for $\varepsilon = 0.2$ and 0.02 (where ε denotes the ratio of j_{hot} to $j_{\parallel}$ in Eq.(12)), where $\eta_0 = 2\Omega$·km. The *in situ* observation of auroral arcs indicates that the contribution of auroral (~5 keV) electrons to the upward current is of minor, say 20 % [*Spiger and Anderson*, 1975]. Thus, the parameter setting of $\varepsilon = 0.2$ is not so unreasonable.

The time evolutions of $\tilde{j}_{\parallel}$, $\tilde{n}$, and Ψ at MLT = 18 and 71.5° for $\varepsilon = 0.2$ (dashed line) and 0.02 (dotted line) are plotted in Figures 9 (a)-(c) along with the result of no ionization case (solid line). The ionization effect for $\varepsilon = 0.02$ becomes noticeably after $t = 20\tau_A$. The perturbation of the ionospheric number density gradually increases to the level of about 40 % of the ambient value, while no remarkable growth is found in the evolutions of $\tilde{j}_{\parallel}$ and Ψ. Thus, the feedback coupling is little affected in the weak ionization case. The ionization effect in the case of $\varepsilon = 0.2$ is more apparent than that of $\varepsilon = 0.02$. In the case of $\varepsilon = 0.2$, after $t = 20\tau_A$, the ionospheric density, as well as the field-aligned current and the field-aligned potential difference, repeats rapid increase and decrease with a period of about 2 τ_A. At the peak of the oscillation the density reaches to 9×10^{10} m^{-3}. The field-aligned current oscillation leads the density oscillation in phase. It is also found that the oscillation period becomes shorter as the amplitude of the density oscillation becomes larger.

The oscillatory development of $\tilde{j}_{\parallel}$ is related to the drift motion of the field-aligned current perturbation which is enhanced by the ionization effect. A contour plot of $\tilde{j}_{\parallel}$ in latitude-time diagram at MLT=18 is shown in Figure 10. At the peak of the periodic enhancement of $\tilde{j}_{\parallel}$ after $t = 28\tau_A$, the intensity of the upward field-aligned current perturbation reaches to $3\mu A/\mathrm{m}^2$ at about 71.6° in latitude. It can be seen that a pair of upward and downward field-aligned current perturbations make a southward drift with a velocity of about 600 m/sec after $t = 20\tau_A$. The

observed southward drift is similar to the Pedersen drift in the linear feedback theory, where an unstable region propagates in the direction of the Pedersen current (southward) with the velocity of $M_P E_\theta/2$ (= 1.1km/sec) [*Sato*, 1978]. The perturbation of $\tilde{j}_{\parallel}$ disappears in the lower latitude region, because the field-aligned current density in that region is insufficient to form a field-aligned potential resulting in ionization. However, it is found that the source term, $(\tilde{j}_{\parallel} + \gamma j_{hot})/eh$, of Eq.(5) is about two times larger than the sink term, $-\alpha\tilde{n}(\tilde{n} + 2N_0)$, when the enhancement of the upward field-aligned current is maximized in each oscillation. Thus, if the field-aligned current distribution is more broadened in the latitudinal direction at the equilibrium state, an auroral arc with an upward field-aligned current perturbation will continue to grow for a longer period, since it can drift for a longer period in the southward direction.

A prominently enhanced density striation appears at MLT = 18. Equi-contours of the ionospheric density enhancement and the field-aligned potential difference at $t = 30.69\tau_A$ are shown in Figures 11 (a) and (b). The large ionospheric density enhancement coincides with the peak of the field-aligned potential difference. Thus, the elongated arc structure with large density enhancement at MLT = 18 can be regarded as a bright auroral arc, because electrons accelerated by the field-aligned potential precipitate there.

By satellite observations in the auroral acceleration region, it is clarified that small-scale field-aligned currents with spatial scales of 5-20 km at the ionospheric altitude are embedded in a large-scale current system in correspondence with localized electron precipitation events [*Burch et al.*, 1983; *Potemra et al.*, 1987; *Fukunishi et al.*, 1991]. The small-scale structures seem to correspond to individual auroral arcs. These observational results are consistent with our simulation results, in which the field-aligned potential difference with the latitudinal width of about 10 km at the ionospheric height accelerates electrons and, thus, enhances the growth of auroral arcs by the ionization effect.

5 Summary

Three dimensional simulations for the magnetosphere-ionosphere coupling system have been carried out in order to study the self-excitation of auroral arcs and the formation of field-aligned potential structure. The results are summarized as follows :

First, the global development of the dark arcs has been examined for four different plasma flow patterns in the magnetospheric equatorial plane. The following features are concluded.

1) Even if the twin-vortex convection pattern is symmetric with respect to the noon-midnight line and to the dawn-dusk line, the appearance of auroral arcs is not symmetric with respect to the both lines. The dawn-dusk asymmetry of the dark-arc distribution originates from the skewed ionospheric current pattern given by the summation of the Pedersen current, anti-symmetric with respect to the noon-midnight plane, and the symmetric Hall current. In addition to the asymmetric feature of the ionospheric current, the recombination effect characterized by the global distribution of the ionospheric density causes a significant difference in the arc formation between the dayside sector and the nightside sector.

2) When the peak of the equilibrium electric potential in the magnetospheric equator, namely, the center of the twin-vortex convection pattern, is shifted towards a lower latitude, the global distribution of the dark arcs makes a marked difference from that for the case where the potential peak is located in a high latitude region. The most active region of the feedback instability has moved from the post-midnight sector on the high latitude side to the evening sector on the low latitude side.

3) Two more simulations with more realistic magnetospheric convection patterns were carried out. One simulation has a twin-vortex flow pattern whose centers are inclined towards the midnight, while the other one has a dawn-dusk asymmetric flow pattern which is more like the ground-based observation and the satellite observation. The dark arcs are predominantly formed in the evening-midnight sector for the former case and in the dusk sector, namely, in the upward field-aligned current region, for the latter case. The apparent difference of the arc distribution in the four simulations implies that the global development of the dark auroral arcs depends largely on the convection pattern in the magnetospheric equator and the background ionospheric density distribution.

Secondly, local developments of auroral arcs are investigated with special interests in 1) nonlinear evolution of dark arcs without field-aligned potentials, 2) stabilization of the feedback instability due to generation of parallel anomalous resistivity, and 3) evolution of auroral arcs including the ionization effect in the ionosphere.

1) The nonlinear recombination, $-\alpha\tilde{n}^2$, plays two important roles in the nonlinear development of dark arcs, i.e., suppression of positive dark arcs (density enhancement) and maintenance

of negative dark arcs (density depletion). Survival of the negative dark arc corresponding to the perturbed downward field-aligned current and suppression of the positive dark arc corresponding to the perturbed upward field-aligned current stimulate a new positive dark arc generation associated with a new upward field-aligned current that is excited to compensate the role of the disappeared primary upward current. The secondary positive dark arc is generated near the survived negative dark arc. In this way, a peculiar disappearance-appearance behavior of auroral arcs can be explained.

2) As the magnitude of the model resistivity, η_0 in Eq.(8), becomes larger, the growth of the feedback instability is found to be more suppressed. It is inferred from the transmission line model of the magnetosphere [*Sato*, 1978] that the nonlinear phase-mismatching due to the parallel resistivity between the ionospheric electric potential and the field-aligned current can reduce the growth rate of the feedback instability. Thus, we can conclude that the growth of a dark auroral arc can be weakened by the generation of parallel resistivity.

3) When the electron-ion pair production rate becomes larger, the arc density and the arc-associated upward field-aligned current are more enhanced, as is naturally expected. More interestingly, a violent periodical appearance of auroral arcs is observed, when the production rate becomes fairly large. Examination of appearance and disappearance of an arc reveals that the period is basically the Alfvén bounce time between the ionosphere and the magnetospheric equator and tends to be shortened as the arc develops.

Thirdly, the parallel resistivity resulting from the enhancement of the upward field-aligned current generates the parallel electric field and, hence, the field-aligned potential difference. This means that a spontaneously excited auroral arc due to the feedback instability in the M-I coupling system is accompanied by a field-aligned potential generation. A V-shaped parallel potential structure with a latitudinal width typically of 10 km at the ionospheric altitude and a potential difference typically of $200V$ is formed in an arc-associated local current system with the development of the local density and upward field-aligned current. Generation of parallel potential in association with the growth of an auroral arc is consistent with recent satellite observations of small-scale structures of the field-aligned currents and the precipitating electron fluxes.

References

Ahn, B.-H., H. W. Kroehl, Y. Kamide, and D. J. Gorney, Estimation of ionospheric electrodynamic parameters using ionospheric conductance deduced from bremsstrahlung X ray image data, *J. Geophys. Res.*, **94**, 2565-2586, 1989.

Atkinson, G., Auroral arcs: result of the interaction of a dynamic magnetosphere with the ionosphere, *J. Geophys. Res.*, **75**, 4746-4755, 1970.

Burch, J. L., P. H. Reiff, and M. Sugiura, Upward electron beams measured by DE-1: a primary source of dayside region-1 Birkeland currents, *Geophys. Res. Lett.*, **8**, 753-756, 1983.

Casserly, R. T. Jr., and P. A. Cloutier, Rocket-based magnetic observations of auroral Birkeland currents in association with a structured auroral arc, *J. Geophys. Res.*, **80**, 2165-2168, 1975.

Cloutier, P. A., B. R. Sandel, H. R. Anderson, P. M. Pazich, and R. J. Spiger, Measurement of auroral Birkeland currents and energetic particle fluxes, *J. Geophys. Res.*, **78**, 640-647, 1973.

Fukunishi, H., R. Fujii, S. Kokubun, F. Tohyama, T. Mukai, and H. Oya, Small-scale field-aligned currents observed by the Akebono (EXOS-D) satellite, *Geophys. Res. Lett.*, **18**, 297-300, 1991.

Ichimaru, S., *Basic principles of plasma physics*, Benjamin, New York, 1973.

Kamide, Y., Y. Ishihara, T. L. Killeen, J. D. Craven, L. A. Frank, and R. A. Heelis, Combining electric field and aurora observations from DE 1 and 2 with ground magnetometer records to estimate ionospheric electromagnetic quantities, *J. Geophys. Res.*, **94**, 6723-6738, 1989.

Lysak, R. L., and C. T. Dum, Dynamics of magnetosphere-ionosphere coupling including turbulent transport, *J. Geophys. Res.*, **88**, 365-380, 1983.

Miura, A., and T. Sato, Numerical simulation of global formation of auroral arcs, *J. Geophys. Res.*, **85**, 73-91, 1980.

Ogawa, T., and T. Sato, New mechanism of auroral arcs, *Planet. Space Sci.*, **19**, 1393-1412, 1971.

Park, R. J., and P. A. Cloutier, Rocket-based measurement of Birkeland currents related to an auroral arc and electrojet, *J. Geophys. Res.*, **76**, 7714-7733, 1971.

Potemra, T. A, L. J. Zanetti, R. E. Erlandson, P. F. Bythrow, G. Gustafsson, M. H. Acuña, and R. Lundin, Observations of large-scale Birkeland currents with Viking, *Geophys. Res. Lett.*, **14**, 419-422, 1987.

Sato, T., A theory of quiet auroral arcs, *J. Geophys. Res.*, **83**, 1042-1048, 1978.

Sato, T., and T. E. Holzer, Quiet auroral arcs and electrodynamic coupling between the ionosphere and the magnetosphere, 1, *J. Geophys. Res.*, **78**, 7314-7329, 1973.

Sato, T., and H. Okuda, Ion-acoustic double layers, *Phys. Rev. Lett.*, **44**, 740-743, 1980.

Sagdeev, R. Z., and A. A. Galeev, *Nonlinear Plasma Theory*, Benjamin, New York, 1969.

Sesiano, J., and P. A. Cloutier, Measurements of field-aligned currents in a multiple auroral arc system, *J. Geophys. Res.*, **81**, 116-122, 1976.

Spiger, R. J. and H. R. Anderson, Electron currents associated with an auroral band, *J. Geophys. Res.*, **80**, 2161-2164, 1975.

Watanabe, K., M. Ashour-Abdalla, and T. Sato, A numerical model of the magnetosphere-ionosphere coupling: preliminary results, *J. Geophys. Res.*, **91**, 6973-6978, 1986.

Watanabe, K., and T. Sato, Self-excitation of auroral arcs in a three-dimensionally coupled magnetosphere-ionosphere system, *Geophys. Res. Lett.*, **15**, 717-720, 1988.

Watanabe, K., and T. Sato, Global simulation of the solar wind-magnetosphere interaction: the importance of its numerical validity, *J. Geophys. Res.*, **95**, 75-88, 1990.

Appendix

The model of anomalous resistivity in our simulation study is based on the quasi-linear theory of the wave-particle interaction. Estimation of the parameter η_0, which represents the magnitude of the anomalous resistivity in the simulation model, is also given in this appendix.

We consider the quasi-linear interaction between the current carrying electrons and the excited ion acoustic waves. The velocity distribution of current carrying electrons $f_0(v)$ suffers from diffusion in the velocity space due to the resonant interaction between the electrostatic waves and the streaming electrons. As is well known, the quasi-linear diffusion is given by

$$\frac{\partial f_0}{\partial t} = \frac{\partial}{\partial v} D(v) \frac{\partial f_0}{\partial v}$$

$$D(v) = (\frac{e}{m_e})^2 \sum_k \pi k^2 |\phi_k|^2 \delta(kv - \omega)$$

$$f_0(v) = \frac{1}{\sqrt{2\pi T_e/m_e}} \exp[-\frac{(v - V_d)^2}{2(T_e/m_e)}]$$

[*Sagdeev and Galeev*, 1969], where k and ω are the wave number and the angular frequency; ϕ_k is the electrostatic potential of ion acoustic waves; m_e and T_e are the electron mass and temperature; V_d is the drift velocity of electrons; $\delta(x)$ is the delta function. The drag force for the current carrying electrons is obtained from the first moment of the above equation, i.e.,

$$\begin{aligned}
\frac{\partial}{\partial t}(n_e m_e V_d) &= n_e m_e \int [v \frac{\partial}{\partial v} D(v) \frac{\partial f_0}{\partial v}] dv \\
&= -\frac{n_e e^2}{m_e} \sum_k \pi k |\phi_k|^2 (\frac{\partial f_0}{\partial v})_{v=\omega/k} \\
&= -\sqrt{2\pi} \omega_p^2 (\frac{T_e}{m_e})^{-3/2} \sum_k \frac{1}{2} \epsilon_0 k |\phi_k|^2 (V_d - \frac{\omega}{k}) \\
&\equiv -\nu n_e m_e (V_d - C_s)
\end{aligned}$$

where $(\omega/k - V_d)^2 \ll T_e/m_e$ is assumed; n_e is the number density of electrons; ν denotes the anomalous collision frequency; $C_s (= \sqrt{T_e/m_i} = \omega/k)$ is the ion acoustic velocity (m_i is the ion mass); ϵ_0 is the dielectric constant. When the wave energy spectrum is approximated by

$$\sum_k \frac{1}{2} \epsilon_0 k |\phi_k|^2 \approx \frac{A}{2} n_e m_e (V_d - V_c)^2 \lambda_D \quad ,$$

then, the anomalous collision frequency is given by

$$\nu \approx A \sqrt{\frac{\pi}{2}} \omega_p \frac{(V_d - V_c)^2}{T_e/m_e} \quad .$$

Here, λ_D denotes the Debye length; V_c and ω_p are the critical velocity of the ion acoustic instability and the angular plasma frequency; A is a non-dimensional constant representing the excited wave energy density. Thus, the anomalous resistivity η is given by

$$\eta = m_e \nu / n_e e^2 \approx \sqrt{\frac{\pi}{2}} \frac{A}{\epsilon_0 \omega_p} \frac{(V_d - V_c)^2}{T_e/m_e} \quad .$$

We apply the above relation to our simulation model. Since the ion acoustic instability would occur where the effect of the ion Landau damping is minor, we take $V_c = C_s$ (see Eq.(9) in section 2.2). According to our simulation model, the anomalous resistivity can be reduced to

$$\begin{aligned} \eta &\approx \sqrt{\frac{\pi}{2}} \frac{A}{\epsilon_0 \omega_p} \frac{m_e}{m_i} \left(\frac{\Delta j}{j_c}\right)^2 \left(\frac{j_{\parallel} - j_c}{\Delta j}\right)^2 \\ &\equiv \eta_0 \left(\frac{j_{\parallel} - j_c}{\Delta j}\right)^2 \quad . \end{aligned}$$

Substituting that $A \sim 1$ and $(\Delta j/j_c)_{r/R_E=c_3} = 0.8$ (see Eq.(10) in section 2.2), we can estimate an approximate value of η_0 with an ambiguity of the plasma frequency of current carrying electrons f_p, i.e.,

$$\eta_0 \sim 8 \times 10^6 / f_p \quad .$$

In the acceleration region of auroral electrons, f_p ranges from 10^3 Hz to 10^4 Hz. Thus, η_0 is estimated to be $8 \times 10^2 \sim 8 \times 10^3 \Omega \cdot$m.

Table 1 Physical parameters used in simulations

Ionospheric magnetic field B_I	-3.1 $\times$ 10^{-5} tesla
Magnetospheric Alfvén velocity V_A	1,000 km/sec
Ionospheric number density (noon) N_{noon}	1 $\times$ 10^{11} m^{-3}
Ionospheric number density (midnight) N_{night}	3 $\times$ 10^{10} m^{-3}
Pedersen mobility M_P	1.6 $\times$ 10^4 m^2/sec·V
Hall mobility M_H	3.2 $\times$ 10^4 m^2/sec·V
Recombination rate α	3×10^{-13} m^3/sec
Alfvén transit time τ_A	57.33 sec
Effective ionospheric height h	12 km

Figure Captions

Figure 1 Global distributions of the perturbed number density (left) and the perturbed field-aligned current density (right) in the ionosphere at (a) $t = 11.28\tau_A$, (b) $t = 16.93\tau_A$, and (c) $t = 22.57\tau_A$. The region between two concentric circles represents the ionospheric region of the simulation system at $r = 1R_E$ from 70° to 72° in latitude. Solid (dashed) line shows the density increment (decrement) and the upward (downward) field-aligned current perturbation. Contour intervals are $6 \times 10^9 \mathrm{m}^{-3}$ for the number density and $6 \times 10^{-7} \mu A/\mathrm{m}^2$ for the current density. (a) A positive dark arc appears near at MLT = 3, and (b) develops significantly with the passage of time. Then, (c) one new positive arc appears on the east side of the original arc, thus making a more longitudinally elongated arc. Simultaneously, another new positive arc is born on the lower latitude side.

Figure 2 Density contours showing the formation and movement of dark auroral arcs in the latitude-time diagram at MLT = 2.84. Increment and decrement of the number density are shown by solid and dashed lines with contour interval of $6 \times 10^9 \mathrm{m}^{-3}$. While drifting in the poleward direction, the first positive arc born at about 71.6° at $t \simeq 5\tau_A$ grows until $t = 16\tau_A$, and then rapidly disappears at about 71.7° at $t \simeq 25\tau_A$. Another positive arc is born at about 71.2° at $t \simeq 17\tau_A$.

Figure 3 Time evolutions of the source and sink terms in Eq.(5) at MLT = 2.84 and 71.64° in latitude, i.e., $\tilde{j}_{\parallel}/eh$ (solid line), $-2\alpha\tilde{n}N_0$ (dashed line), $-\alpha\tilde{n}^2$ (dotted line), and $-\alpha\tilde{n}(\tilde{n} + 2N_0)$ (dot-dashed line).

Figure 4 Equilibrium patterns of the electric potential and the field-aligned current density in the ionosphere. Panels (a)-(d), respectively, correspond to the cases I $\sim$ IV. The simulation zone is viewed from a point in the midnight meridian plane. As the electric potential changes from negative to positive, color changes from blue to red. Intensity of the field-aligned current is depicted by the white (upward) and black (downward) contour lines.

Figure 5 Global distributions of the positive dark arc at about $t = 11\tau_A$ for the cases I $\sim$ IV. Light-bluish zone corresponds to the ionospheric boundary zone. Color changes from blue to white through yellow as the ionospheric density increases.

Figure 6 (a) Field-aligned potential difference contours and (b) total field-aligned current density contours at $t = 29.79\tau_A$ where the anomalous resistivity effect is taken into account, i.e., $\eta_0 = 2\Omega$·km. Contour levels in (a) are defined as $10V$, $50V$, $100V$, and $150V$. Solid and dashed lines in (b) show upward and downward field-aligned currents with contour interval of $2.5\mu A/\mathrm{m}^2$.

Figure 7 Latitudinal profiles of (a) the ionospheric density perturbation and (b) the field-aligned current density perturbation in the ionosphere at MLT = 18 at $t = 29.79\tau_A$ for $\eta_0 = 2\Omega$·km. (c) Generated field-aligned potential contours and (d) generated anomalous resistivity contours in the meridian plane at MLT = 18. Contour levels in (c) are defined as $-10V$, $-50V$, $-100V$, and $-150V$, and the contour interval in (d) is 5Ω·m.

Figure 8 Time evolutions of (a) the perturbed number density, (b) the perturbed field-aligned current density, and (c) the field-aligned potential difference at MLT = 18 and 71.5° in latitude for $\eta_0 = 0$ (solid line), 0.4 (dot-dashed line), 2 (dashed line), and 10 (dotted line) Ω·m.

Figure 9 Same as Figures 8 (a)-(c) for $\eta_0 = 2\Omega$·m when the ionization effect is taken into account where $\varepsilon = 0$ (solid line), 0.02 (dotted line), and 0.2 (dashed line). Note the appearance of the oscillatory behavior in the auroral arc formation when the ionization rate is strong ($\varepsilon = 0.2$).

Figure 10 Density contours showing the rapid and periodical generation of bright auroral arcs in the latitude-time diagram at MLT = 18 for $\varepsilon = 0.2$. Upward and downward perturbations of the current density are represented by the solid and dashed lines with contour interval of $6 \times 10^{-7} A/\mathrm{m}^2$.

Figure 11 Distributions of (a) the ionospheric density increment (solid line) and decrement (dashed line) and (b) the field-aligned potential difference at $t = 30.69\tau_A$ for $\varepsilon = 0.2$. Contour interval of $1.8 \times 10^{10}\mathrm{m}^{-3}$ in (a) is three times larger than that of Figures 1(a)-(c). Contour levels in (b) are defined in the same way as those in Figure 6(a). The most enhanced density structure (bright auroral arc) appearing at MLT = 18 (left panel) reflects the enhancement of the parallel potential difference appearing at MLT = 18 (right panel).

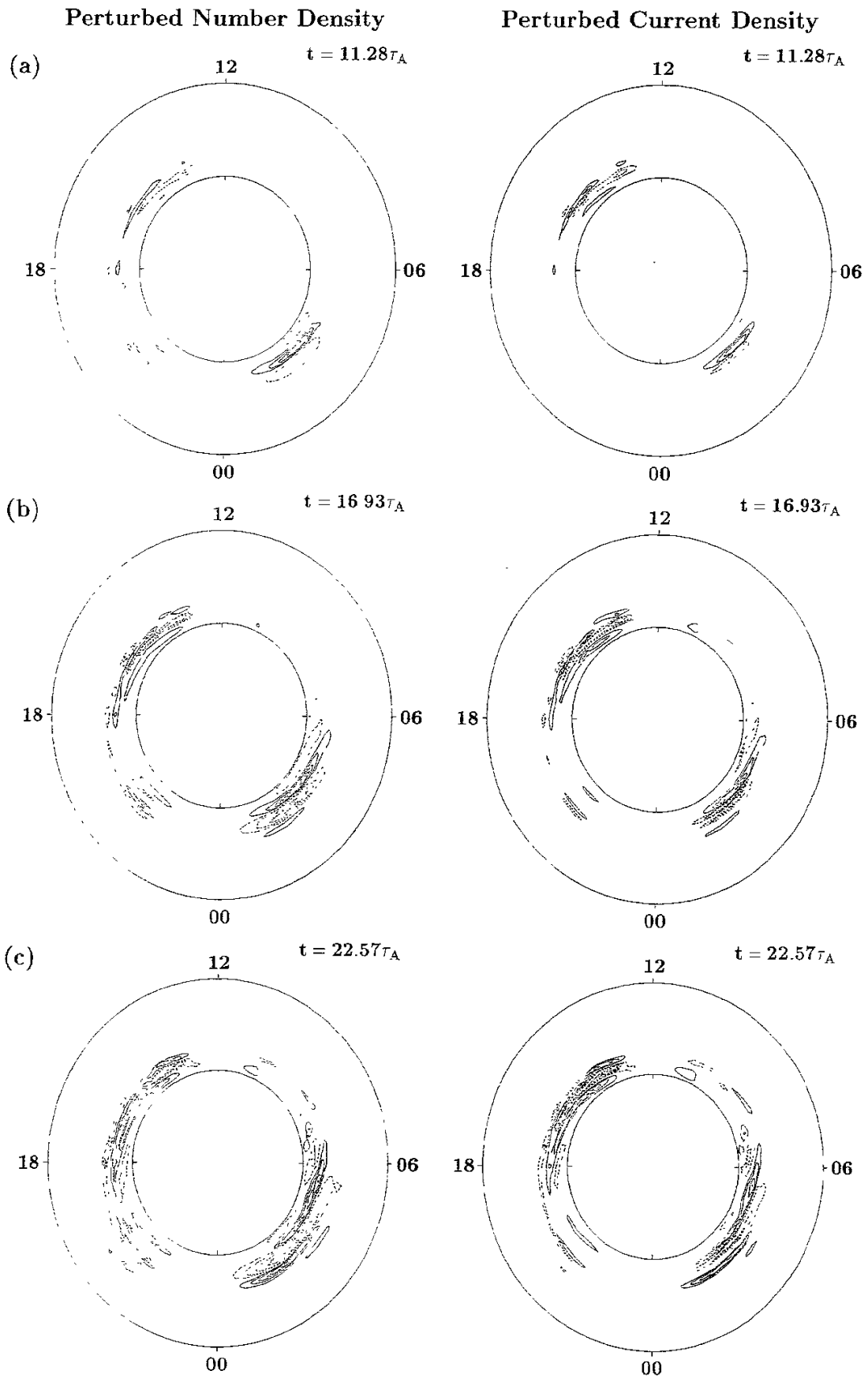
Perturbed Number Density
Perturbed Current Density
(a)
t = 11.28τ_A
t = 11.28τ_A
(b)
t = 16 93τ_A
t = 16.93τ_A
(c)
t = 22.57τ_A
t = 22.57τ_A
12
18
06
00

Figure 1

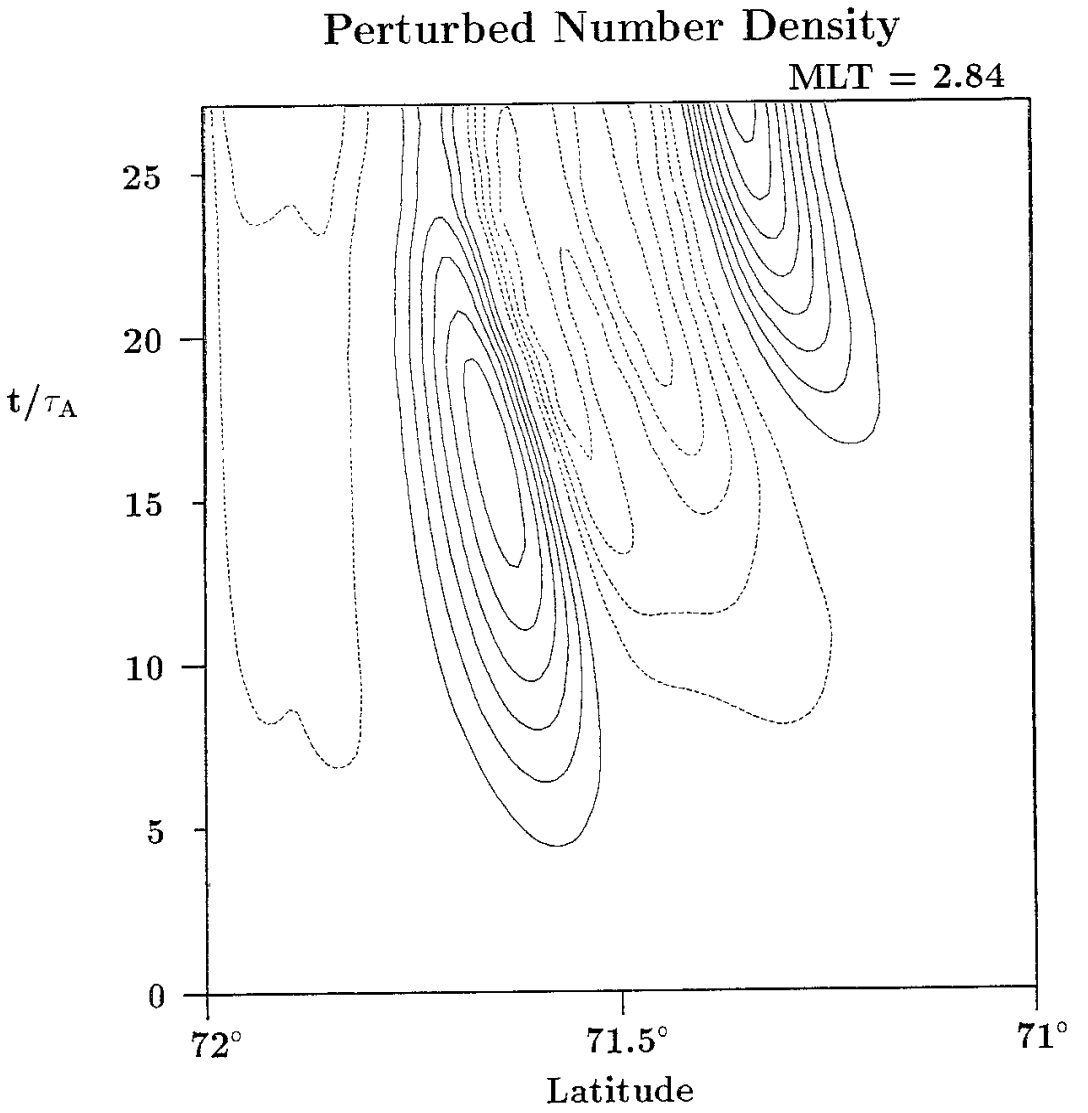
Perturbed Number Density
MLT = 2.84
25
20
15
10
5
0
t/τA
72°
71.5°
71°
Latitude

Figure 2

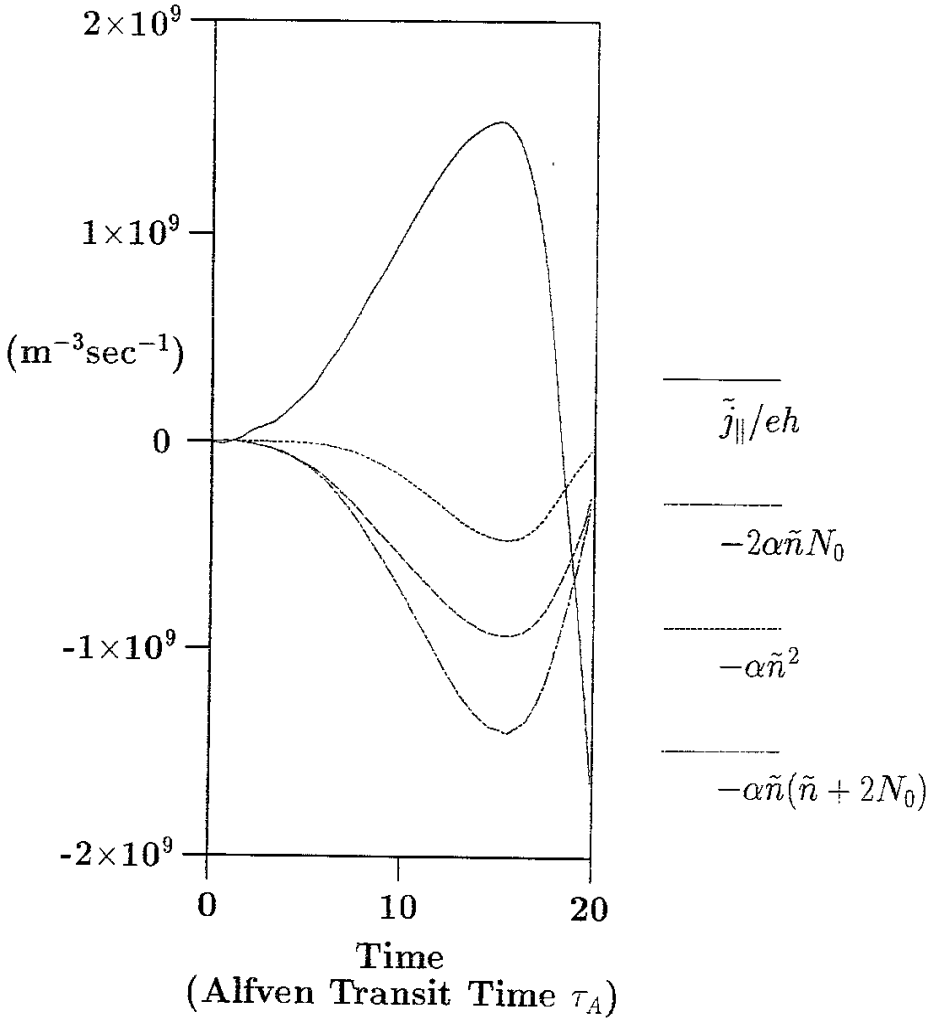
2×10^9
1×10^9
(m^-3sec^-1)
0
-1×10^9
-2×10^9
0
10
20
Time
(Alfven Transit Time τ_A)
j̃_∥/eh
−2αñN_0
−αñ^2
−αñ(ñ + 2N_0)

Figure 3

Figures 4 (a)-(d)

Figures 5 (a)-(d)

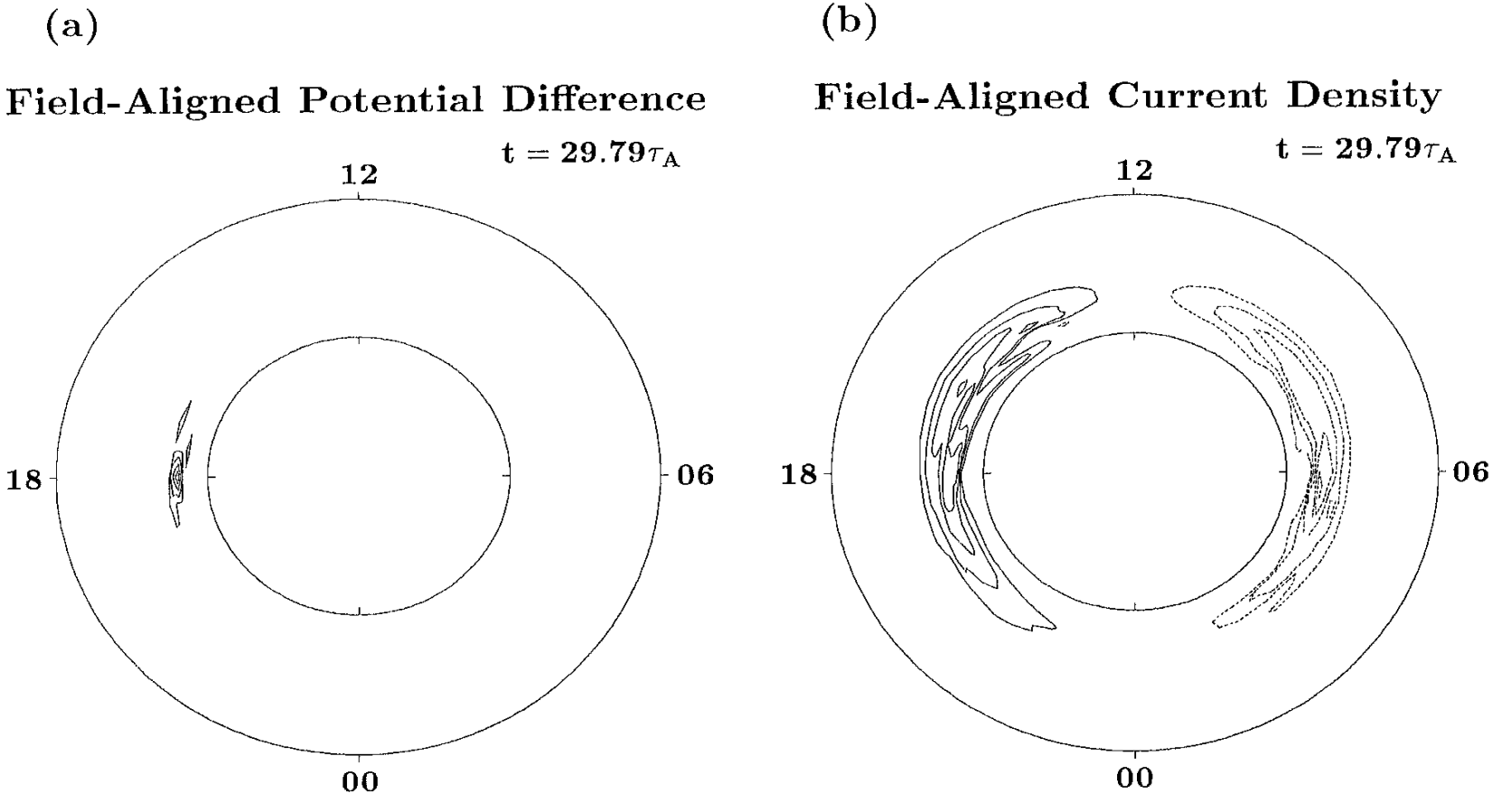

Figures 6 (a) and (b)

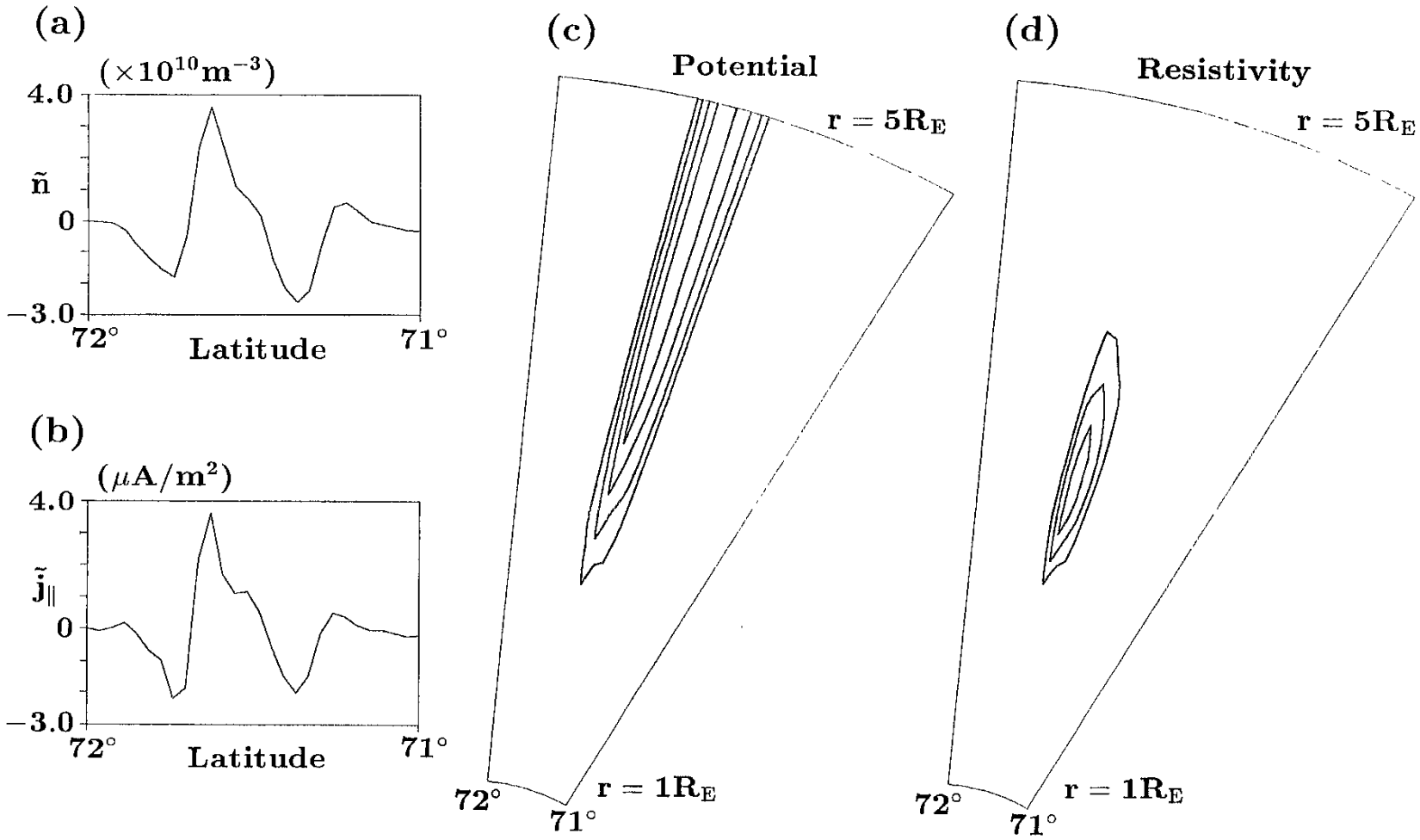
(a)
$(\times 10^{10}\mathrm{m}^{-3})$
4.0
$\tilde{n}$
0
−3.0
72°
Latitude
71°
(b)
$(\mu\mathrm{A/m}^2)$
4.0
$\tilde{j}_{\parallel}$
0
−3.0
72°
Latitude
71°
(c)
Potential
r = 5R$_E$
72°
71°
r = 1R$_E$
(d)
Resistivity
r = 5R$_E$
72°
71°
r = 1R$_E$

Figures 7 (a)-(d)

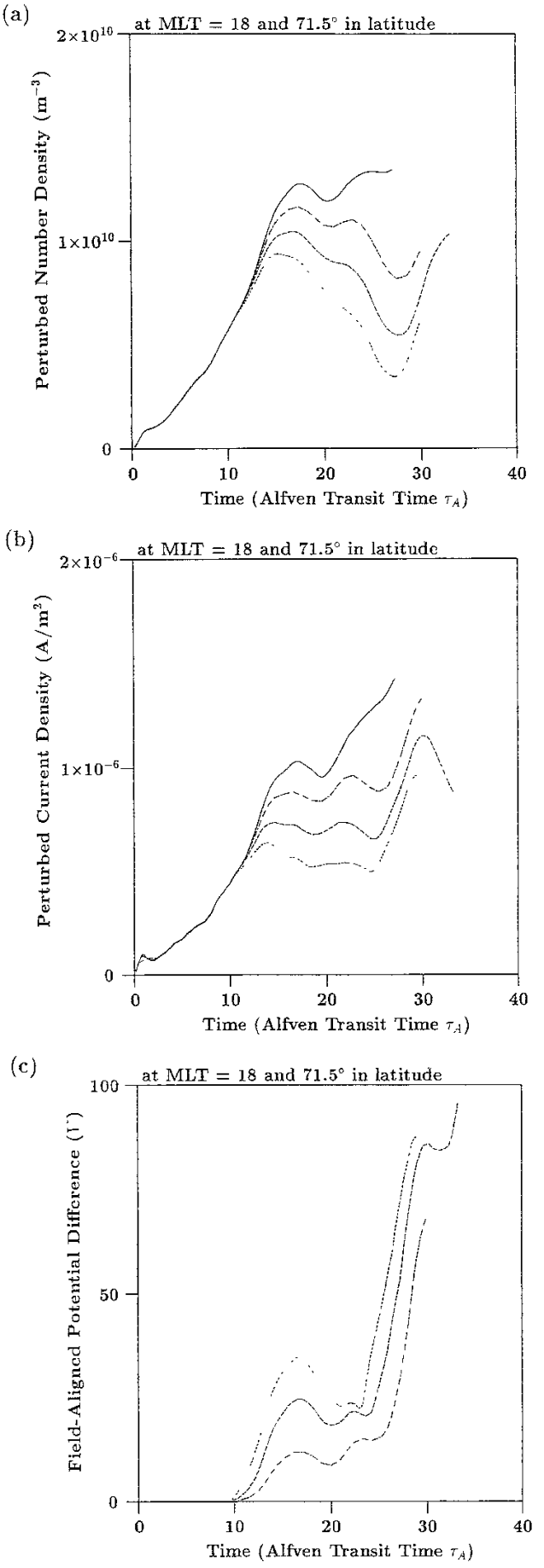
(a)
at MLT = 18 and 71.5° in latitude
2×10^10
1×10^10
0
Perturbed Number Density (m^-3)
0
10
20
30
40
Time (Alfven Transit Time τ_A)
(b)
at MLT = 18 and 71.5° in latitude
2×10^-6
1×10^-6
0
Perturbed Current Density (A/m^2)
0
10
20
30
40
Time (Alfven Transit Time τ_A)
(c)
at MLT = 18 and 71.5° in latitude
100
50
0
Field-Aligned Potential Difference (V)
0
10
20
30
40
Time (Alfven Transit Time τ_A)

Figures 8 (a)-(c)

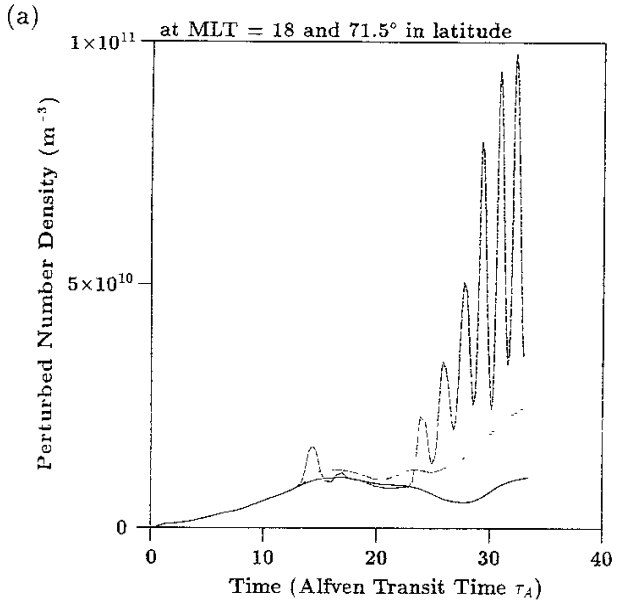
(a)
at MLT = 18 and 71.5° in latitude
Perturbed Number Density (m^{-3})
1×10^{11}
5×10^{10}
0
0
10
20
30
40
Time (Alfven Transit Time τ_A)

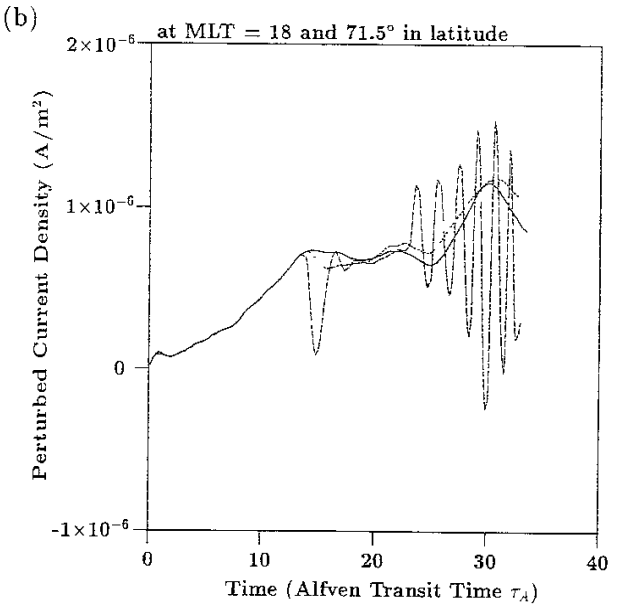
(b)
at MLT = 18 and 71.5° in latitude
Perturbed Current Density (A/m^2)
2×10^{-6}
1×10^{-6}
0
-1×10^{-6}
0
10
20
30
40
Time (Alfven Transit Time τ_A)

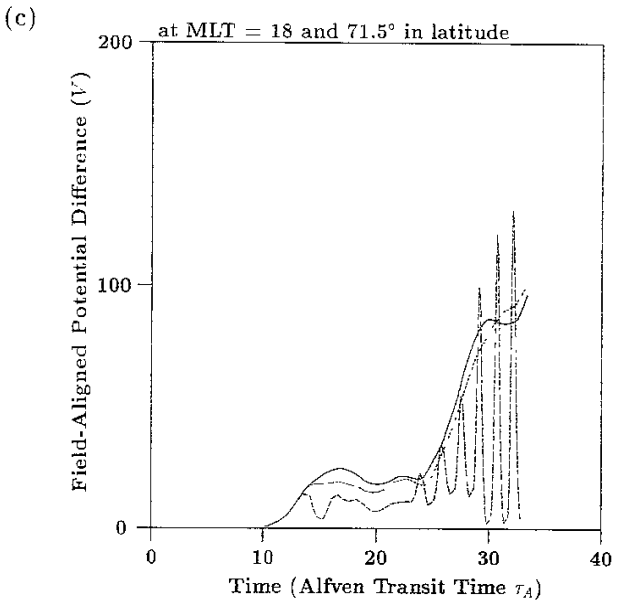
(c)
at MLT = 18 and 71.5° in latitude
Field-Aligned Potential Difference (V)
200
100
0
0
10
20
30
40
Time (Alfven Transit Time τ_A)

Figures 9 (a)-(c)

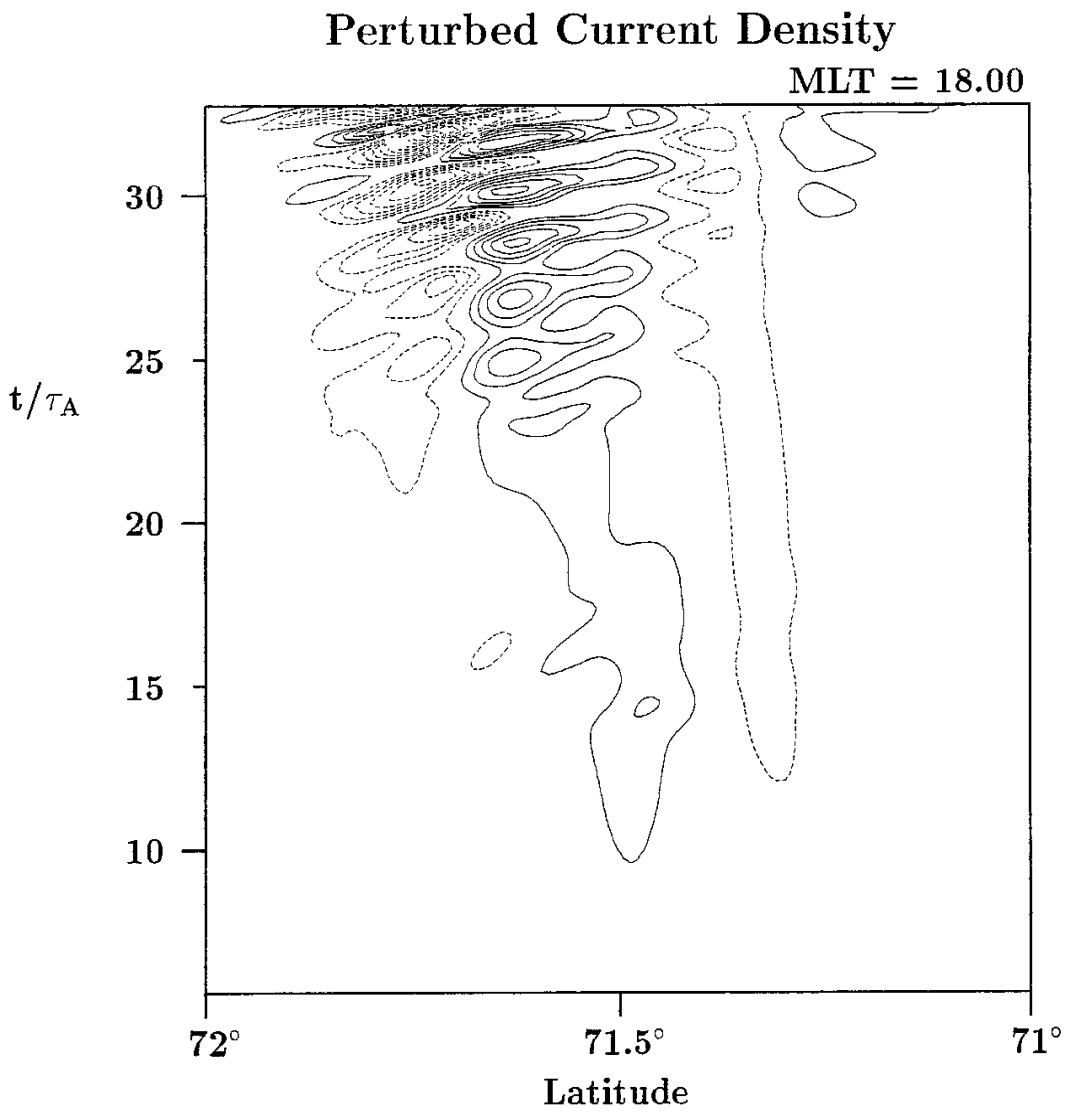
Perturbed Current Density
MLT = 18.00
30
25
20
15
10
t/τA
72°
71.5°
71°
Latitude

Figure 10

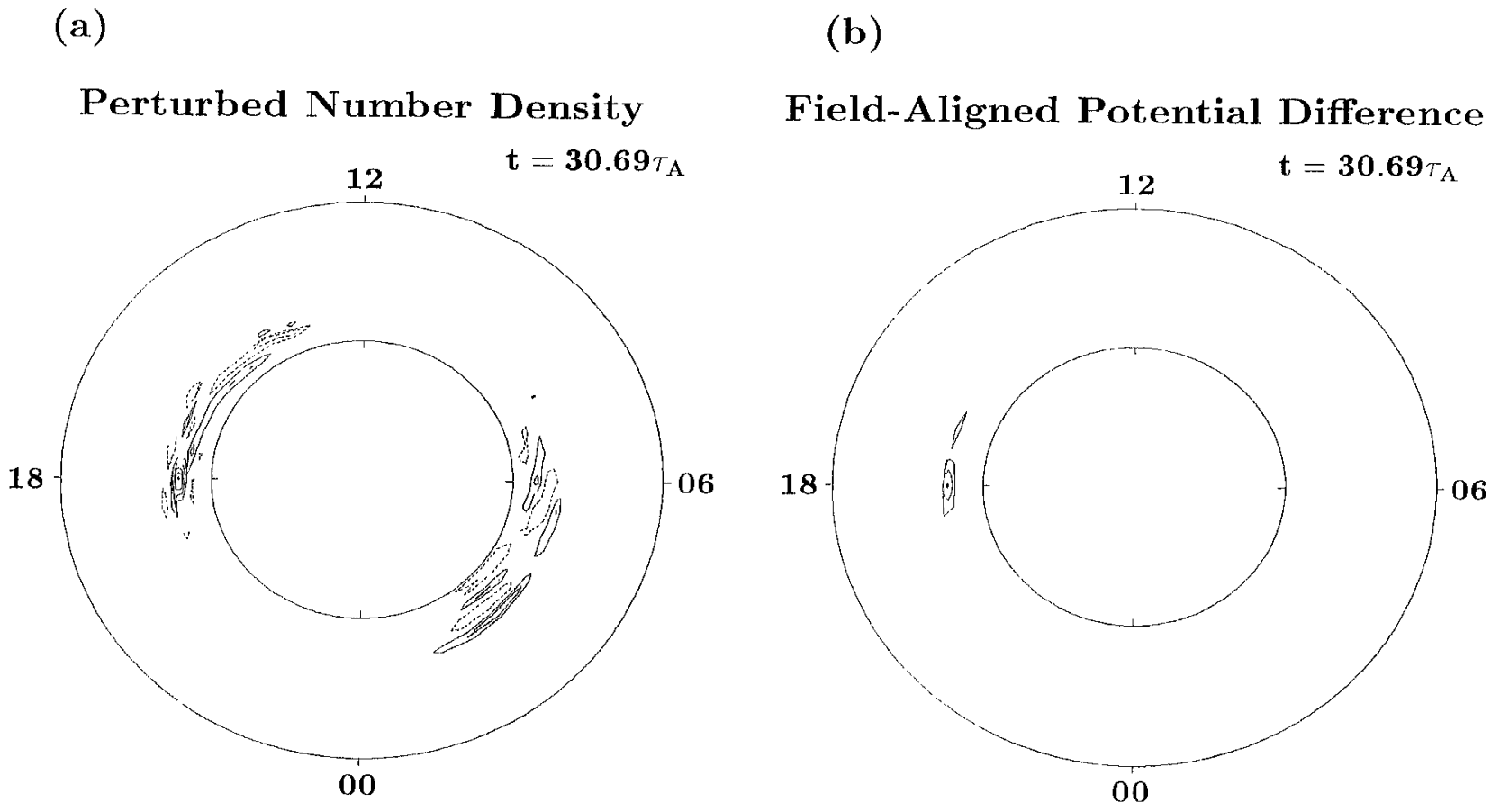

Figures 11 (a) and (b)

Recent Issues of NIFS Series

NIFS-153 Sergey V. Bazdenkov and T. Sato, *On a Ballistic Method for Double Layer Regeneration in a Vlasov-Poisson Plasma*; Jun. 1992

NIFS-154 J. Todoroki, *On the Lagrangian of the Linearized MHD Equations*; Jun. 1992

NIFS-155 K. Sato, H. Katayama and F. Miyawaki, *Electrostatic Potential in a Collisionless Plasma Flow Along Open Magnetic Field Lines;* Jun. 1992

NIFS-156 O.J.W.F.Kardaun, J.W.P.F.Kardaun, S.-I. Itoh and K. Itoh, *Discriminant Analysis of Plasma Fusion Data*; Jun. 1992

NIFS-157 K. Itoh, S.-I. Itoh, A. Fukuyama and S. Tsuji, *Critical Issues and Experimental Examination on Sawtooth and Disruption Physics*; Jun. 1992

NIFS-158 K. Itoh and S.-I. Itoh, *Transition to H-Mode by Energetic Electrons*; July 1992

NIFS-159 K. Itoh, S.-I. Itoh and A. Fukuyama, *Steady State Tokamak Sustained by Bootstrap Current Without Seed Current*; July 1992

NIFS-160 H. Sanuki, K. Itoh and S.-I. Itoh, *Effects of Nonclassical Ion Losses on Radial Electric Field in CHS Torsatron/Heliotron*; July 1992

NIFS-161 O. Motojima, K. Akaishi, K. Fujii, S. Fujiwaka, S. Imagawa, H. Ji, H. Kaneko, S. Kitagawa, Y. Kubota, K. Matsuoka, T. Mito, S. Morimoto, A. Nishimura, K. Nishimura, N. Noda, I. Ohtake, N. Ohyabu, S. Okamura, A. Sagara, M. Sakamoto, S. Satoh, T. Satow, K. Takahata, H. Tamura, S. Tanahashi, T. Tsuzuki, S. Yamada, H. Yamada, K. Yamazaki, N. Yanagi, H. Yonezu, J. Yamamoto, M. Fujiwara and A. Iiyoshi, *Physics and Engineering Design Studies on Large Helical Device*; Aug. 1992

NIFS-162 V. D. Pustovitov, *Refined Theory of Diamagnetic Effect in Stellarators;* Aug. 1992

NIFS-163 K. Itoh, *A Review on Application of MHD Theory to Plasma Boundary Problems in Tokamaks*; Aug. 1992

NIFS-164 Y.Kondoh and T.Sato, *Thought Analysis on Self-Organization Theories of MHD Plasma*; Aug. 1992

NIFS-165 T. Seki, R. Kumazawa, T. Watari, M. Ono, Y. Yasaka, F. Shimpo, A. Ando, O. Kaneko, Y. Oka, K. Adati, R. Akiyama, Y. Hamada,

S. Hidekuma, S. Hirokura, K. Ida, A. Karita, K. Kawahata, Y. Kawasumi, Y. Kitoh, T. Kohmoto, M. Kojima, K. Masai, S. Morita, K. Narihara, Y. Ogawa, K. Ohkubo, S. Okajima, T. Ozaki, M. Sakamoto, M. Sasao, K. Sato, K. N. Sato, H. Takahashi, Y. Taniguchi, K. Toi and T. Tsuzuki, *High Frequency Ion Bernstein Wave Heating Experiment on JIPP T-IIU Tokamak*; Aug. 1992

NIFS-166 Vo Hong Anh and Nguyen Tien Dung, *A Synergetic Treatment of the Vortices Behaviour of a Plasma with Viscosity*; Sep. 1992

NIFS-167 K. Watanabe and T. Sato, *A Triggering Mechanism of Fast Crash in Sawtooth Oscillation*; Sep. 1992

NIFS-168 T. Hayashi, T. Sato, W. Lotz, P. Merkel, J. Nührenberg, U. Schwenn and E. Strumberger, *3D MHD Study of Helias and Heliotron;* Sep. 1992

NIFS-169 N. Nakajima, K. Ichiguchi, K. Watanabe, H. Sugama, M. Okamoto, M. Wakatani, Y. Nakamura and C. Z. Cheng, *Neoclassical Current and Related MHD Stability, Gap Modes, and Radial Electric Field Effects in Heliotron and Torsatron Plasmas;* Sep. 1992

NIFS-170 H. Sugama, M. Okamoto and M. Wakatani, *K- ε Model of Anomalous Transport in Resistive Interchange Turbulence* ; Sep, 1992

NIFS-171 H. Sugama, M. Okamoto and M. Wakatani, *Vlasov Equation in the Stochastic Magnetic Field* ; Sep. 1992

NIFS-172 N. Nakajima, M. Okamoto and M. Fujiwara, *Physical Mechanism of E_{ψ}-Driven Current in Asymmetric Toroidal Systems* ; Sep.1992

NIFS-173 N. Nakajima, J. Todoroki and M. Okamoto, *On Relation between Hamada and Boozer Magnetic Coordinate System* ; Sep. 1992

NIFS-174 K. Ichiguchi, N. Nakajima, M. Okamoto, Y. Nakamura and M. Wakatani, *Effects of Net Toroidal Current on Mercier Criterion in the Large Helical Device* ; Sep. 1992

NIFS-175 S. -I. Itoh, K. Itoh and A. Fukuyama, *Modelling of ELMs and Dynamic Responses of the H-Mode* ; Sep. 1992

NIFS-176 K. Itoh, S.-I. Itoh, A. Fukuyama, H. Sanuki, K. Ichiguchi and J. Todoroki, *Improved Models of β-Limit, Anomalous Transport and Radial Electric Field with Loss Cone Loss in Heliotron / Torsatron* ; Sep. 1992

NIFS-177 N. Ohyabu, K. Yamazaki, I. Katanuma, H. Ji, T. Watanabe, K. Watanabe, H. Akao, K. Akaishi, T. Ono, H. Kaneko, T. Kawamura,

Y. Kubota, N. Noda, A. Sagara, O. Motojima, M. Fujiwara and A. Iiyoshi, *Design Study of LHD Helical Divertor and High Temperature Divertor Plasma Operation* ; Sep. 1992

NIFS-178 H. Sanuki, K. Itoh and S.-I. Itoh, *Selfconsistent Analysis of Radial Electric Field and Fast Ion Losses in CHS Torsatron / Heliotron* ; Sep. 1992

NIFS-179 K. Toi, S. Morita, K. Kawahata, K. Ida, T. Watari, R. Kumazawa, A. Ando, Y. Oka, K. Ohkubo, Y. Hamada, K. Adati, R. Akiyama, S. Hidekuma, S. Hirokura, O. Kaneko, T. Kawamoto, Y. Kawasumi, M. Kojima, T. Kuroda, K. Masai, K. Narihara, Y. Ogawa, S. Okajima, M. Sakamoto, M. Sasao, K. Sato, K. N. Sato, T. Seki, F. Shimpo, S. Tanahashi, Y. Taniguchi, T. Tsuzuki, *New Features of L-H Transition in Limiter H-Modes of JIPP T-IIU* ; Sep. 1992

NIFS-180 H. Momota, Y. Tomita, A. Ishida, Y. Kohzaki, M. Ohnishi, S. Ohi, Y. Nakao and M. Nishikawa, *D-^{3}He Fueled FRC Reactor "Artemis-L"* ; Sep. 1992

NIFS-181 T. Watari, R. Kumazawa, T. Seki, Y. Yasaka, A. Ando, Y. Oka, O. Kaneko, K. Adati, R. Akiyama, Y. Hamada, S. Hidekuma, S. Hirokura, K. Ida, K. Kawahata, T. Kawamoto, Y. Kawasumi, S. Kitagawa, M. Kojima, T. Kuroda, K. Masai, S. Morita, K. Narihara, Y. Ogawa, K. Ohkubo, S. Okajima, T. Ozaki, M. Sakamoto, M. Sasao, K. Sato, K. N. Sato, F. Shimpo, H. Takahashi, S. Tanahasi, Y. Taniguchi, K. Toi, T. Tsuzuki and M. Ono, *The New Features of Ion Bernstein Wave Heating in JIPP T-IIU Tokamak*; Sep, 1992

NIFS-182 K. Itoh, H. Sanuki and S.-I. Itoh, *Effect of Alpha Particles on Radial Electric Field Structure in Torsatron / Heliotron Reactor*; Sep. 1992

NIFS-183 S. Morimoto, M. Sato, H. Yamada, H. Ji, S. Okamura, S. Kubo, O. Motojima, M. Murakami, T. C. Jernigan, T. S. Bigelow, A. C. England, R. S. Isler, J. F. Lyon, C. H. Ma, D. A. Rasmussen, C. R. Schaich, J. B. Wilgen and J. L. Yarber, *Long Pulse Discharges Sustained by Second Harmonic Electron Cyclotron Heating Using a 35GH$_Z$ Gyrotron in the Advanced Toroidal Facility*; Sep. 1992

NIFS-184 S. Okamura, K. Hanatani, K. Nishimura, R. Akiyama, T. Amano, H. Arimoto, M. Fujiwara, M. Hosokawa, K. Ida, H. Idei, H. Iguchi, O. Kaneko, T. Kawamoto, S. Kubo, R. Kumazawa, K. Matsuoka, S. Morita, O. Motojima, T. Mutoh, N. Nakajima, N. Noda, M. Okamoto, T. Ozaki, A. Sagara, S. Sakakibara, H. Sanuki, T. Saki, T. Shoji, F. Shimbo, C. Takahashi, Y. Takeiri, Y. Takita, K. Toi, K. Tsumori, M. Ueda, T. Watari, H. Yamada and I. Yamada, *Heating Experiments Using Neutral Beams with Variable Injection Angle and ICRF Waves in CHS* ; Sep. 1992

NIFS-185 H. Yamada, S. Morita, K. Ida, S. Okamura, H. Iguchi, S. Sakakibara, K. Nishimura, R. Akiyama, H. Arimoto, M. Fujiwara, K. Hanatani, S. P. Hirshman, K. Ichiguchi, H. Idei, O. Kaneko, T. Kawamoto, S. Kubo, D. K. Lee, K. Matsuoka, O, Motojima, T. Ozaki, V. D. Pustovitov, A. Sagara, H. Sanuki, T. Shoji, C. Takahashi, Y. Takeiri, Y. Takita, S. Tanahashi, J. Todoroki, K. Toi, K. Tsumori, M. Ueda and I. Yamada, *MHD and Confinement Characteristics in the High-β Regime on the CHS Low-Aspect-Ratio Heliotron / Torsatron* ; Sep. 1992

NIFS-186 S. Morita, H. Yamada, H. Iguchi, K. Adati, R. Akiyama, H. Arimoto, M. Fujiwara, Y. Hamada, K. Ida, H. Idei, O. Kaneko, K. Kawahata, T. Kawamoto, S. Kubo, R. Kumazawa, K. Matsuoka, T. Morisaki, K. Nishimura, S. Okamura, T. Ozaki, T. Seki, M. Sakurai, S, Sakakibara, A. Sagara, C. Takahashi, Y. Takeiri, H. Takenaga, Y. Takita, K. Toi, K. Tsumori, K. Uchino, M. Ueda, T. Watari, I. Yamada, *A Role of Neutral Hydrogen in CHS Plasmas with Reheat and Collapse and Comparison with JIPP T-IIU Tokamak Plasmas* ; Sep. 1992

NIFS-187 K. Ioth, S.-I. Itoh, A. Fukuyama, M. Yagi and M. Azumi, *Model of the L-Mode Confinement in Tokamaks* ; Sep. 1992

NIFS-188 K. Itoh, A. Fukuyama and S.-I. Itoh, *Beta-Limiting Phenomena in High-Aspect-Ratio Toroidal Helical Plasmas*; Oct. 1992

NIFS-189 K. Itoh, S. -I. Itoh and A. Fukuyama, *Cross Field Ion Motion at Sawtooth Crash* ; Oct. 1992

NIFS-190 N. Noda, Y. Kubota, A. Sagara, N. Ohyabu, K. Akaishi, H. Ji, O. Motojima, M. Hashiba, I. Fujita, T. Hino, T. Yamashina, T. Matsuda, T. Sogabe, T. Matsumoto, K. Kuroda, S. Yamazaki, H. Ise, J. Adachi and T. Suzuki, *Design Study on Divertor Plates of Large Helical Device (LHD)* ; Oct. 1992

NIFS-191 Y. Kondoh, Y. Hosaka and K. Ishii, *Kernel Optimum Nearly-Analytical Discretization (KOND) Algorithm Applied to Parabolic and Hyperbolic Equations* : Oct. 1992

NIFS-192 K. Itoh, M. Yagi, S.-I. Itoh, A. Fukuyama and M. Azumi, *L-Mode Confinement Model Based on Transport-MHD Theory in Tokamaks* ; Oct. 1992

NIFS-193 T. Watari, *Review of Japanese Results on Heating and Current Drive* ; Oct. 1992

NIFS-194 Y. Kondoh, *Eigenfunction for Dissipative Dynamics Operator and Attractor of Dissipative Structure* ; Oct. 1992